https://doi.org/10.5194/wes-2026-41
Preprint. Discussion started: 17 February 2026

eawe european academy of wind energy
Open Access WIND ENERGY SCIENCE DISCUSSIONS

Experimental investigation of harmonic surge motions on the far wake of a wind turbine model and analysis of a resulting subharmonic wake response

Antonin Hubert[1], Boris Conan[1], and Sandrine Aubrun[1]
[a]Nantes Université, École Centrale Nantes, CNRS, LHEEA, UMR 6598, F-44000 Nantes, France
Correspondence: Boris Conan (boris.conan@ec-nantes.fr) and Sandrine Aubrun (sandrine.aubrun@ec-nantes.fr)

Abstract.

As the number of floating offshore wind farm projects grows across the world, several questions remain unanswered in the domain of floating wind turbine wakes. Previous studies observed that the motions impact the wake under laminar inflow conditions, and that the modifications are observable even under high turbulent inflow conditions, that are more realistic. However, these spatiotemporal behavior modifications still require precise characterization, especially under turbulent conditions. Thus, the present article aims to extend the previous work by studying the wake dynamics induced by surge motion under turbulent inflow, and to find the frequency and the spatiotemporal characteristics related to this motion. For this purpose, a porous disk is placed in a wind tunnel with a high level of turbulent inflow, and some experiments are performed at $8.125D$ (D the turbine diameter) downwind of the disk. First, hot-wire measurements are used to identify a 'critical' frequency at which wake dynamics are the greatest, and, then, stereo-PIV measurements are conducted for this frequency configuration to characterize the spatiotemporal wake dynamics. The results indicate a critical Strouhal number of approximately $St = 0.24$, for which the surge motion induces periodic contraction and expansion of the wake at the same frequency as the imposed motion. A quasi-steady-state analysis reveals that these modifications are larger than the predictions of basic wake models, highlighting the dynamic nature of the wake response. Moreover, inclined surge-generated periodic coherent structures are observed during this work, which are supposed to be related to shear effects. Additionally, an unexpected subharmonic frequency peak appears in the far wake velocity spectra. POD and coherence analyses suggest that this is related to a far wake meandering phenomenon, locked onto this subharmonic frequency.

1 Introduction

Since the first wind turbine, attributed to J. Blyth in the late 19th century, the understanding of their wake has steadily increased, and nowadays those of a fixed wind turbine appear to be well-known (Ainslie, 1988; Vermeer et al., 2003; Larsen, 2007; Porté-Agel et al., 2020). In the context of growing global energy demand, wind turbines were installed offshore with a monopile or 4-legged jacket foundation. Unlike onshore, this environment offers substantial advantages such as unobstructed wind flow and stronger winds, resulting in a higher capacity factor for installed wind turbines (42-55% for new offshore installations vs 30-35% for new onshore ones (Costanzo et al., 2025)). However, as the distance from the coast increases, the cost of turbine

https://doi.org/10.5194/wes-2026-41
Preprint. Discussion started: 17 February 2026

eawe european academy of wind energy
Open Access WIND ENERGY SCIENCE DISCUSSIONS

support structures rises, leading to a technical and economic water depth limit established to approximately 50 m. Therefore, in order to exploit further locations from the coast, and thus, more attractive ones, a new technology with floaters has emerged: the floating offshore wind turbine (FOWT).

FOWTs, in addition to several major offshore challenges, deal with floating motions. They are defined as those of a ship, with surge, sway, and heave translations, and pitch, roll, and yaw rotations. The most widely studied motions are surge and pitch, as they represent the predominant aligned wind-wave case (Porchetta et al., 2019). In order to study their influence, floating motions are often reduced to harmonic functions with a motion amplitude A and a motion frequency f, which can be normalized with turbine and airflow parameters, yielding the normalized amplitude $A^* = \frac{A}{D}$ and the Strouhal number $St = \frac{fD}{U_{\text{hub}}}$ (D the turbine diameter, and U_{hub} the averaged streamwise velocity at hub height). Thus, they can be divided into two categories: the high amplitude and low frequency ones ($A^* \approx 0.1$, $St < 0.3$), relative to the non-linear coupling between the floater and the mooring lines (Leimeister et al., 2018), and the low amplitude and high frequency ($A^* \approx 0.01$, $St > 0.5$), typically caused by the linear response of the floater to wave solicitations (Feist et al., 2021).

Several numerical and experimental studies have investigated the effects of imposed or free motions on the FOWT wake characteristics. The FOWT-specific perspectives began to be analyzed in the 2010s, with Sebastian and Lackner (2011, 2012, 2013). They introduced a wake model, the free vortex method, and showed that the different types of FOWT present significant unsteady aerodynamic loading for high frequency motions ($St > 0.5$). The first wind tunnel investigations were performed by Rockel et al. (2014) with measurements in the wake of a reduced-scale wind turbine subjected to free pitch motion, where the model was mounted on a support that allows free pitch oscillations, resulting in $A \in [16, 19]°$ and $St \in [0.05, 0.07]$. They performed condition averaging triggered by an 18.5° pitch angle and observed a strong impact of the motion, with a global wake deflection upwards. Thus, floating motions appear to have a great influence on FOWT wakes. Since these first studies, more recent works have been performed, and several observations have been made according to the motion characteristics.

(i) First, floating motions impact the mean wake by increasing wake recovery through the addition of turbulence, thereby enhancing turbulent mixing in the flow. Fu et al. (2019, 2020) carried out pitch motion experiments ($A = [5, 10, 20]°$, $St \in [0.0085, 0.28]$) in the case of low-turbulence inflows. They observed a faster wake recovery for imposed motion cases compared to the fixed case, which they attributed to greater shear layer instabilities at the wake border. Moreover, Kopperstad et al. (2020) performed wind tunnel experiments and numerical simulations of the wake of a wind turbine mounted on a barge and on a spar, under uniform low and high turbulent inflow conditions with realistic mooring line motions ($St < 0.25$), resulting in a combination of $A^* \in [0, 0.32]$ surge and $A \in [0, 9]°$ pitch. They showed that the high pitch and surge platform motion amplitudes of the barge concept generate strong coherent flow structures, thereby causing shear layer instabilities at the wake edge, which result in faster wake recovery. Later, Fu et al. (2023) computed numerical simulations of a reduced-scale model of a FOWT subjected to pitch motion of different amplitudes ($A = [1, 4, 10]°$) and with a high Strouhal number ($St = 1.1$). They found that wake recovery is enhanced with motion, caused by tip and root vortex instabilities.

(ii) Second, fore-aft motions induce a 'pulsing' phenomenon at the motion frequency, with a modulation of the wake surface and of the velocity within the wake. Bayati et al. (2018); Fontanella et al. (2021) performed wind tunnel experiments with a turbine model subjected to surge motion ($A^* \in [0.04, 0.06]$, $St \in [0.25, 4]$), and showed an impact on the tip vortices and, by

https://doi.org/10.5194/wes-2026-41
Preprint. Discussion started: 17 February 2026

eawe european academy of wind energy
Open Access WIND ENERGY SCIENCE DISCUSSIONS

extension, the near wake, by adding energy to the wake. Duan et al. (2022) performed a numerical study on a FOWT subjected to surge motion ($A^* \in [0.01, 0.06]$, $St \in [0.56, 2.23]$), and observed the formation of periodic vortex rings in its wake that broke down in the far wake. Based on a stability numerical analysis, Kleine et al. (2022) showed that motion impacts the tip vortices by exciting vortex instability modes depending on the studied motion. Thus, surge motion induces vortices that merge into one large structure coherent in the azimuthal direction. Fu et al. (2023) observed a similar phenomenon with vortex merging in the case of pitch motions and noted that the higher the motion amplitude, the greater its impact. Messmer et al. (2024) studied with wind tunnel experiments a reduced-scale wind turbine under surge motions in a low-turbulence intensity wind ($I \approx 0.3\%$). They showed that surge motions lead to streamwise *pulses* in the wake for $St \in [0.25, 0.5]$.

However, Messmer et al. (2024) observed another phenomenon in the FOWT wake subjected to surge motion. Indeed, a wake meandering appears for motion with $St \in [0.5, 0.9]$. This phenomenon was also observed by Duan et al. (2022) for a wind turbine model moving at $St = 0.55$; the far wake swings regularly at a frequency nearly half that of the motion. These effects are visible for the majority of the tested motion amplitudes but do not appear at higher Strouhal numbers.

Moreover, Kleine et al. (2022) noticed that pitch motion shows a combination of heave and surge effects: the vortex merging appears in the streamwise direction as surge, but vortices at the top tip coalesce faster than those at the bottom tip, approaching heave effects.

(iii) Finally, side-to-side motions imply large translations of the far wake at the motion frequency. Meng et al. (2022) inspected sway motions with low-frequencies ($A^* = [0.1, 0.2]$, $St \in [0.003, 0.008]$) and showed, using condition-averaging, a wake shift in the direction of the motion compared to its mean position, which gradually decreases with distance. Li et al. (2022) studied the wake of a FOWT subjected to sway and roll motions using large-eddy simulations and linear stability analysis in uniform and low turbulent inflow conditions ($I < 4\%$). The results reveal that the turbine motion of $St \in [0.2 : 0.6]$ can trigger a large-scale far wake meandering even with low amplitudes ($A^* = 0.01$). As Li et al. (2022), Messmer et al. (2024) found that sway motions result in a quasi-periodic meandering phenomenon.

Considering these results, floating motion appears to have a significant impact on the FOWT wake. However, all the previously cited studies are performed under a uniform and low-turbulence level inflow, which is the simplest case. Therefore, actual FOWTs extract energy from the atmospheric boundary layer (ABL), with non-uniform turbulence and velocity profiles, adding complexity to the flow-structure interaction - *e.g.* Counihan (1975); ESDU (1985); VDI (2000). Indeed, previous studies on bottom-fixed wind turbines have shown that the shear present in the inflow can impact the tip vortices by extending the distance between them according to their vertical position in the ABL (Lu and Porté-Agel, 2011; Kleusberg et al., 2019). Thus, it is essential to analyze the FOWT wake under more realistic conditions.

Belvasi et al. (2022); Schliffke et al. (2024) performed wind tunnel measurements with a porous disk subjected to low-frequency heave, surge, and pitch motions ($St \in [0.13, 0.38]$) under realistic turbulent inflow conditions. They observed clear signatures of the harmonic motion frequencies in the spectra of the wake parameters, such as the wake center and the available wind power. These signatures reached a maximum amplification in the studied frequency range. However, they did not distinguish any wake dynamics due to the high level of turbulence in the inflow. Under the same experimental conditions, Raibaudo

https://doi.org/10.5194/wes-2026-41
Preprint. Discussion started: 17 February 2026

eawe european academy of wind energy
Open Access WIND ENERGY SCIENCE DISCUSSIONS

et al. (2023) analyzed the wake of a porous disk subjected to surge motions using the proper orthogonal decomposition (POD) and concluded that these motions do not have a significant impact on the structures of the wake modes.

Using phase-averaging processing, Hubert et al. (2024b) observed different wake dynamics depending on the motion, in line with previous studies involving laminar inflow. Indeed, heave motion ($A^* = 0.03, St = 0.09$) induces a global translation of the wake in the vertical direction; surge motion ($A^* = 0.06, St = 0.11$) imposes modulations on the crosswise wake surface, accompanied by wake available wind power modulations in phase opposition; and pitch motion ($A^* = 4°, St = [0.14, 0.28]$) involves a combination of heave and surge motion effects. Moreover, a quasi-steady-state analysis with basic wake models was performed, showing that the observed spatiotemporal wake behaviors appear to be amplified and are not simply passively advected by the flow. Using phase-averaging from numerical simulation results of a turbine subjected to surge motions with much higher Strouhal numbers ($A^* \in [0.11, 0.44]$, $St \in [3.5, 14]$), Li et al. (2024) observed periodic coherent structures induced in the wake, which appear to enhance the mean wake recovery.

Moreover, Hubert et al. (2024a) conducted wind tunnel experiments on a porous disk subjected to heave and surge step motions under two turbulent inflow conditions. They used a conditional averaging method based on the motion signal and applied it to the wake velocity at $8.125D$ downstream of the turbine model, showing that the inflow conditions barely changed the transient times of the wake. Thus, they found advection velocities of $U_a \approx 0.7U_{hub}$ for ascent step, and $U_a \approx 0.8U_{hub}$ for the descent and surge step motions.

As seen in the present introduction, the effects of motion on the FOWT wakes are still not fully understood, even in low turbulent inflows, and more in-depth work is required. The main purpose of the present work is to contribute to refine the characteristics of the wake of a FOWT under surge motion and to extract the related wake dynamics.

First, the 'critical' Strouhal number, for which the wake dynamics are the greatest, is determined by a spectral analysis based on hot-wire measurements performed $8.125D$ downwind of a porous disk subjected to surge motions. Then, the spatiotemporal wake behavior is investigated using stereo-PIV (S-PIV) experiments for the given critical Strouhal number. In order to facilitate the wake dynamics observation, all experiments are performed with low shear and limited ground effect. As in Hubert et al. (2024b), the dynamics of the wake center position, the wake surface, and the available wind power are analyzed using a phase-averaged method in the fixed and moving frames of reference (FFoR and MFoR). Finally, an unexpected subharmonic signature, observed during the spectral analysis of the wake flow, is studied using coherence functions and POD.

Thus, Sect. 2 presents the methodology used in the present article, including the experimental conditions and the processing tools. The results are described in Sect. 3 and discussed in Sect. 4. Finally, a conclusion is provided in Sect. 5.

https://doi.org/10.5194/wes-2026-41
Preprint. Discussion started: 17 February 2026

eawe european academy of wind energy
Open Access WIND ENERGY SCIENCE DISCUSSIONS

2 Methodology

2.1 Experimental setup

2.1.1 Atmospheric boundary layer physical modeling

All tested cases are conducted in the atmospheric boundary layer wind tunnel at LHEEA (Research Laboratory in Hydrodynamics, Energetics and Atmospheric Environment), a 24 m long and 2×2 m^2 cross-section facility. Figure 1 presents the experimental setup used in this study, where perforated metal plates are placed on the ground and a trip and spires are installed at the entrance of the wind tunnel, permitting the development of a fully developed turbulent boundary layer reproducing a 1:500 neutral marine ABL. The porous disk is located 19 m from the test section entrance.

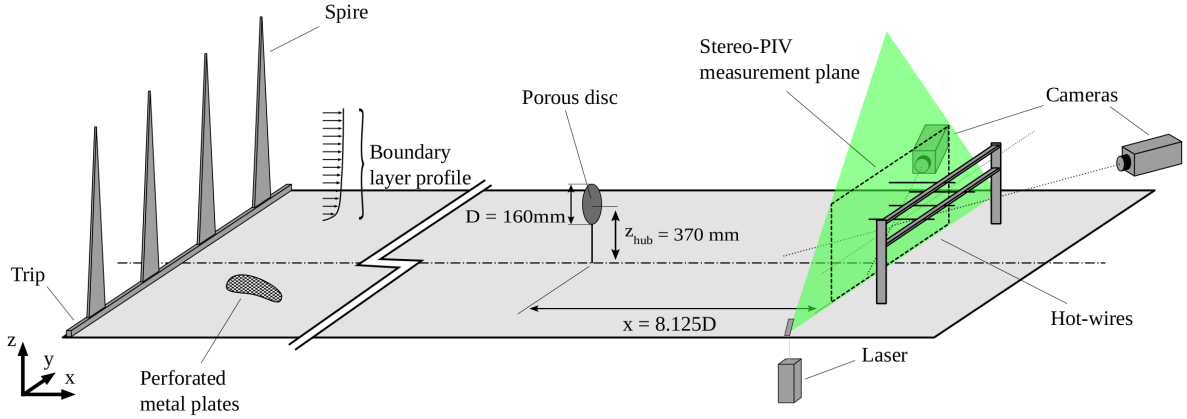

Figure 1. Experimental setup in the atmospheric boundary layer wind tunnel at LHEEA (Research Laboratory in Hydrodynamics, Energetics and Atmospheric Environment). This figure is not fully representative as hot-wire and S-PIV experiments are not performed simultaneously.

Figure 2 shows the normalized mean streamwise velocity $U_{\mathrm{ABL}}(z)/U_{\mathrm{hub}}$, with $U_{\mathrm{hub}} = 3.4$ m/s, the wind speed at hub height, and the three turbulence intensity profiles $I_{\mathrm{i}}(z) = \frac{\sigma_{\mathrm{i}}(z)}{U_{\mathrm{ABL}}(z)}$, with σ_{i} the standard deviation of the velocity i-component. The resulting velocity and turbulence intensity profiles, summarized in Table 1, correspond to a neutral ABL developed on a slightly rough terrain (VDI, 2000; Counihan, 1975). At full scale, this is equivalent to an aerodynamic roughness length of $z_0 = 5.7\times\ 10^{-3}$ and an integral length scale of ${}^{x}L_u = 260$ m. The turbine model, a porous disk of diameter $D = 160$ mm, is positioned in the upper part of the ABL, at $z_{\mathrm{hub}} = 370$ mm, where the shear is low and the ground has a limited effect on the wake. This configuration, which facilitates wake dynamic observations, was made simpler on purpose to be compared to a realistic configuration in the lower part of the ABL, as performed in Hubert et al. (2024b). The Reynolds number based on the disk diameter is $Re = \frac{U_{hub}D}{\nu} = 3.5\times10^4$, with $\nu = 15.6\times10^{-6}$ being the kinematic viscosity of the air, which allows for validating the assumption of Reynolds number independence (Chamorro et al., 2012; Schliffke, 2022). Table 1 summarizes the inflow parameter values of the present study in comparison to those of Hubert et al. (2024b); Schliffke et al. (2024) performed

https://doi.org/10.5194/wes-2026-41
Preprint. Discussion started: 17 February 2026

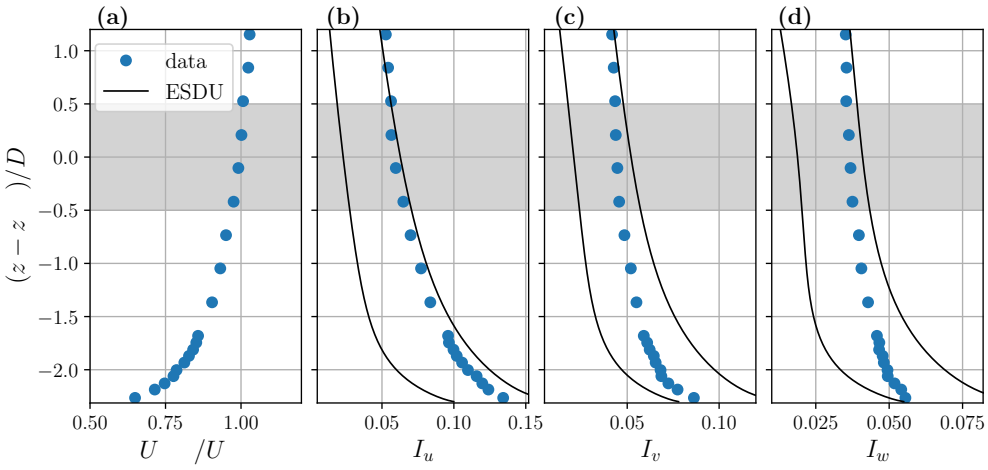

Figure 2. Normalized mean streamwise velocity profile in the wind tunnel **(a)** and turbulence intensity profiles in the streamwise **(b)**, transversal **(c)** and vertical **(d)** direction. The gray areas represent the turbine model height range and the black lines represent the range of turbulence intensity expected for a slightly rough terrain ESDU (1985). Figure inspired from Schliffke et al. (2024).

in the same modeled ABL. More details about the experimental setup and the characteristics of the inflow are provided in Schliffke et al. (2024) and Hubert et al. (2024b).

Table 1. Inflow parameters of the present study compared to Hubert et al. (2024b).

Parameters	Model-scale	Model-scale (Hubert et al., 2024b)
Hub height z_{hub}	370 mm	120 mm
Streamwise velocity at hub height U_{hub}	3.4 m/s	2.9 m/s
Turbulence intensity at hub height $[I_u, I_v, I_w]$	[0.058,0.045,0.037]	[0.091, 0.057, 0.044]
Integral length-scale of turbulence at hub height ${}^{x}L_u$	520 mm	480 mm
Roughness length z_0	1.15×10^{-5} m	1.15×10^{-5} m
ABL power-law exponent α	0.11	0.11
Zero-plane displacement d_0	0 m	0 m

2.1.2 Measurement systems

Two measurement systems are used in this study: hot-wire probes and S-PIV, both measuring velocity at $8.125D$ downstream of the porous disk (Fig. 1), corresponding to previous similar studies performed by Belvasi et al. (2022); Schliffke (2022); Schliffke et al. (2024); Hubert et al. (2024b). Moreover, this value is in agreement with an actual full-scale distance between two turbines in a wind farm (Dalla Longa et al., 2018).

https://doi.org/10.5194/wes-2026-41
Preprint. Discussion started: 17 February 2026

eawe european academy of wind energy
Open Access WIND ENERGY SCIENCE DISCUSSIONS

The hot-wire system consists of four Dantec 55-P11 probes (referred to as HW1-4), equipped with a 5 μm diameter and 1.25 mm long tungsten wire, positioned in the test section of the wind tunnel, according to Fig. 3. They are calibrated every day in the free flow of the wind tunnel with a reference Pitot tube. The King's law coefficients (King, 1914) are estimated using a best-fit approach with temperature and pressure corrections, resulting in a fit goodness value of about $\chi^2 = 1 \times 10^{-3}$. The hot-wires primarily measure the streamwise velocity component at an acquisition frequency of 15 kHz (the axis of the sensors is aligned with the y-direction) during an acquisition time of 1800 s. A Butterworth filter with a cut-off frequency of 1 kHz is applied to the hot-wire measurements in order to reduce high-frequency noise.

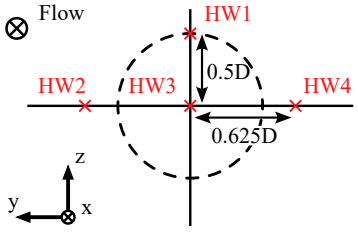

Figure 3. Hot-wire location (red) in the wind tunnel compared to the porous disk position (dashed black circle).

The S-PIV system includes a Laskin nozzle seeder positioned upstream of the spires (Fig. 1) and spraying oil droplets of about 1 μm, a Nd-YAG double cavity laser (2×200 mJ) emitting two pulses with a wavelength of 532 mm at a time delay of 350 μs and an emission rate of 14.1 Hz, and two sCMOS 5.5 Mpx HighSense Zyla cameras with 60 mm Nikon objective lenses and 6.5 μm pixel size installed on the same side of the test section (Fig. 1). For each tested case, 14,000 image pairs are acquired. The persistent background is removed by subtracting the mean field, and a three-pass adaptive correlation from a 128 px $\times$ 128 px to a 32 px $\times$ 32 px interrogation window with a 50% overlap is performed on the resulting images. Finally, vector field pairs are combined to reconstruct the velocity fields, providing the three velocity components in the plane (y, z), normal to the flow.

The measurement uncertainties depend on the experimental setup and are difficult to calculate; however, some estimations are provided. For hot-wires, it is a combination of the uncertainties of the instrumentation, the calibration equipment, and the experimental conditions, such as temperature and pressure. During the calibration, the total uncertainty is estimated to 3% (Dynamics, 2004). The uncertainty of the pressure sensor connected to the Pitot tube is given by the manufacturers, who predict a precision of $\pm 5\%$ of the measurement. Concerning the S-PIV, the total measurement uncertainty depends on the measurement chain used and is relative to the experimental setup and the postprocessing algorithms (Raffel et al., 1998; Wieneke, 2017; Sciacchitano, 2019). However, a highly simplistic typical value states that the measurement uncertainty of the particle displacement is approximately 0.1 pixel units (Adrian and Westerweel, 2011).

https://doi.org/10.5194/wes-2026-41
Preprint. Discussion started: 17 February 2026

eawe european academy of wind energy
Open Access WIND ENERGY SCIENCE DISCUSSIONS

2.1.3 Model description and test conditions

The model used in the present article is a porous disk - considered as a far wake generator (Vermeer et al., 2003; Aubrun et al., 2019) - with a solidity of $\sigma = 57\%$, slightly below the limit for which the vortex shedding phenomenon appears behind a solid body, which gives a thrust coefficient of $C_{\mathrm{T}} = 0.65$ and a representative power coefficient of $C_{\mathrm{P}} = 0.25$ (Aubrun et al., 2019).

The motion cases investigated in this study are harmonic surge motions with amplitudes and frequencies summarized in Tab. 2, in addition to a reference fixed case. Their amplitudes A_{motion} are defined over time t, as:

$$A_{\mathrm{motion}}(t) = A \sin(2\pi f t) \tag{1}$$

with A and f, the amplitude and the frequency of the motion, respectively. Cases are separated into two parts: the measurement campaign for the frequency impact study, using hot-wires ($\mathbf{HW}_{\#}$), and that for the wake dynamics study using S-PIV ($\mathbf{SPIV}_{\#}$). As defined in Sect. 1, two normalized quantities are used in the present study: the normalized amplitude $A^* = \frac{A}{D}$ and the Strouhal number $St = \frac{fD}{U_{\mathrm{hub}}}$.

Table 2. Parameters of the harmonic motions imposed to the wind turbine model.

Case	Motion	A [mm]	A^*	f [Hz]	St
$\mathbf{HW_0}$	fixed	–	–	–	–
$\mathbf{HW_{0.14}}$				3	0.14
$\mathbf{HW_{0.19}}$				4	0.19
$\mathbf{HW_{0.21}}$				4.5	0.21
$\mathbf{HW_{0.22}}$				4.75	0.22
$\mathbf{HW_{0.24}}$	surge	10 mm	0.06	5	0.24
$\mathbf{HW_{0.25}}$				5.25	0.25
$\mathbf{HW_{0.26}}$				5.5	0.26
$\mathbf{HW_{0.28}}$				6	0.28
$\mathbf{HW_{0.33}}$				7	0.33
$\mathbf{SPIV_0}$	fixed	–	–	–	–
$\mathbf{SPIV_{0.14}}$				3	0.14
$\mathbf{SPIV_{0.24}}$	surge	10 mm	0.06	5	0.24
$\mathbf{SPIV_{0.28}}$				6	0.28

2.2 Data processing

2.2.1 Estimation of the motion impacts

The impact of each motion case on the far wake turbulent characteristics is analyzed using the normalized and premultiplied power spectral density of the longitudinal velocity component, measured by hot-wire anemometers, and processed with the

https://doi.org/10.5194/wes-2026-41
Preprint. Discussion started: 17 February 2026

eawe european academy of wind energy
Open Access WIND ENERGY SCIENCE DISCUSSIONS

Welch method. It is defined by:

$$E^* = \frac{fE}{\sigma^2_{U_{\text{hub}}}} \tag{2}$$

where E is the power spectral density (PSD) of the hot-wire velocity, f the frequency, and $\sigma_{U_{\text{hub}}}$ the standard deviation of the velocity measurement in the inflow at hub height. Similarly to Schliffke et al. (2024), the analysis is also performed with the normalized and premultiplied PSD difference between the motion and the fixed cases, representing the energy gain brought by the porous disk motion compared to the fixed case. It is given by:

$$E^* - E^*_{\text{fixed}} = \frac{f(E - E_{\text{fixed}})}{\sigma^2_{U_{\text{hub}}}}. \tag{3}$$

HW1, located at the top part of the wake, is preferred for the following discussions because of its higher response to motion compared to the other hot-wires, as seen in Schliffke et al. (2024).

2.2.2 Proper orthogonal decomposition

The snapshot method, proposed by Sirovich (1987), is applied in this article using the MODULO Pure-Python library. More details of the theory behind the POD are available in Holmes et al. (1996) and Pedersen and Meyer (2002), and more information on the MODULO library can be found in Mendez et al. (2019) and in Ninni and Mendez (2020).

The data matrix of the velocity components $U(x,t)$ is divided in $R = \text{rank}(U)$ energetic modes $M_r(x,t)$, defined as:

$$U = \sum_{r=1}^{R} M_r = \sum_{r=1}^{R} \sigma_r \chi_r \psi_r^{\text{T}} = X \Sigma \Psi^{\text{T}} \tag{4}$$

where r is the index of the energetic mode, σ_r, χ_r, and ψ_r are the amplitude, spatial structure, and temporal structure vectors of the r^{th} mode, respectively, and Σ, X, and Ψ are the amplitude, spatial, and temporal matrices, respectively. The three components of the velocity fields u, v, and w are arranged in U as:

$$U = \begin{bmatrix} u(x_1,t_1) & \dots & u(x_{n_x},t_1) \\ \vdots & & \vdots \\ u(x_1,t_{n_t}) & \dots & u(x_{n_x},t_{n_t}) \\ v(x_1,t_1) & \dots & v(x_{n_x},t_1) \\ \vdots & & \vdots \\ v(x_1,t_{n_t}) & \dots & v(x_{n_x},t_{n_t}) \\ w(x_1,t_1) & \dots & w(x_{n_x},t_1) \\ \vdots & & \vdots \\ w(x_1,t_{n_t}) & \dots & w(x_{n_x},t_{n_t}) \end{bmatrix} \tag{5}$$

χ_r are calculated first, and ψ_r are reconstructed, giving the temporal behavior of the spatial modes.

https://doi.org/10.5194/wes-2026-41
Preprint. Discussion started: 17 February 2026

eawe european academy of wind energy
Open Access WIND ENERGY SCIENCE DISCUSSIONS

2.2.3 Metrics for wake dynamic analysis

The wake parameters used in this article are processed as illustrated in Fig. 4. Two velocity fields are investigated in this article: $\widetilde{\Delta u}$, the phase-averaged velocity deficit field in the fixed frame of reference (FFoR), and $\widetilde{\Delta u_{\mathrm{m}}}$, the phase-averaged velocity deficit field in the moving frame of reference (MFoR). The MFoR is the frame following the wake center at each time step, using the wake center detection methodology defined in Hubert et al. (2024b) - *i.e.* the weighted geometric center (WGC) estimation method. From these results, the phase-averaged wake center coordinates $(\widetilde{y_{\mathrm{c}}}, \widetilde{z_{\mathrm{c}}})$, estimated using the Gaussian fitting method, the phase-averaged wake contours and the phase-averaged wake surface $\widetilde{S_{\mathrm{wk}}}$, defined by the threshold velocity deficit $U_{\mathrm{thresh}} = 0.1U_{\mathrm{hub}}$, are determined for each phase ϕ in MFoR to avoid the bias present in FFoR on statistics in the presence of wake movement.

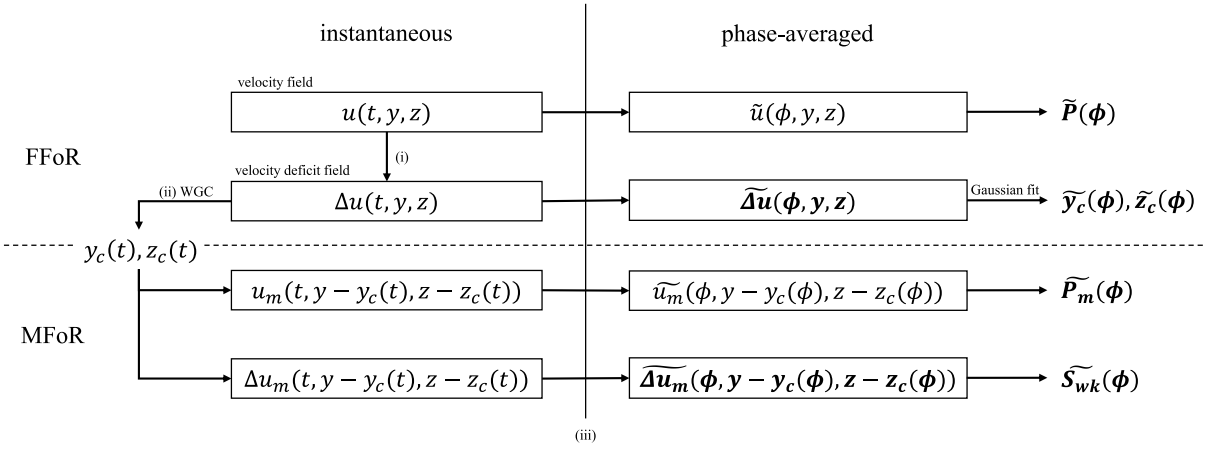

Figure 4. Schematic view of the wake parameters used in this work and their connections. Boxed parameters are velocity fields and bold ones are analyzed in this paper. (i) subtraction of the mean velocity field, (ii) calculation of the wake center positions with the WGC method, and (iii) phase-averaging with kernel smoothing applied on the velocity fields.

The phase-averaged available wind power in FFoR $\widetilde{P}$ and in MFoR $\widetilde{P_{\mathrm{m}}}$ are integrated over a crosswise surface equal to the disk surface S_{disk}, for each phase ϕ, using the following formulas, respectively:

$$\widetilde{P}(\phi) = \int_{S_{\mathrm{disk}}} \frac{1}{2}\rho\widetilde{u}(\phi,y,z)^3 ds \tag{6}$$

and,

$$\widetilde{P_{\mathrm{m}}}(\phi) = \int_{S_{\mathrm{disk}}} \frac{1}{2}\rho\widetilde{u_{\mathrm{m}}}(\phi,y-y_{\mathrm{c}}(\phi),z-z_{\mathrm{c}}(\phi))^3 ds \tag{7}$$

with ρ the air density, and $\widetilde{u}(\phi,y,z)$ and $\widetilde{u_{\mathrm{m}}}(\phi,y-y_{\mathrm{c}}(\phi),z-z_{\mathrm{c}}(\phi))$ the phase-averaged velocity fields in FFoR and MFoR, respectively. $\widetilde{P}$ represents the available wind power a downstream turbine could be subjected to, and $\widetilde{P_{\mathrm{m}}}$ the actual wind power

https://doi.org/10.5194/wes-2026-41
Preprint. Discussion started: 17 February 2026

eawe european academy of wind energy
Open Access WIND ENERGY SCIENCE DISCUSSIONS

within the wake. Both are normalized by the available wind power in the inflow P_{ABL}, also integrated on the disk surface:

$$P_{\text{ABL}} = \int_{S_{\text{disk}}} \frac{1}{2}\rho U_{\text{ABL}}(y,z)^3 ds \tag{8}$$

A large part of the data processing used in this article is the same as in Hubert et al. (2024b), where more details about the WGC and the Gaussian fitting methods, used to estimate the wake center positions, the FFoR and MFoR differences, and the phase-averaging method with kernel smoothing are available.

3 Results analysis

3.1 Determination of the most impactful Strouhal number for the surge motion

Figure 5 presents E^* of the HW1 velocity (a) and $E^* - E^*_{\text{fixed}}$ for the different surge cases (b). All motion cases exhibit a clear signature at the motion frequency, indicating an impact of the porous disk on its wake dynamics, as seen in previous studies (Belvasi et al., 2022; Schliffke et al., 2024). For the range tested, the intensity of the spectral signature depends on the Strouhal number. The range of Strouhal numbers tested was chosen to refine around the peak of the response.

Additionally, a second signature, lower but broader than that at the motion frequency, has been observed during the experimentation, especially visible for $\mathbf{HW_{0.28}}$ in Fig. 5, with a maximum at half the motion frequency. The cause of this secondary peak is studied in Sect. 3.3.

Figure 6 presents the maximum energy levels attained by the frequency peak associated with the surge motion for each case tested and for each HW. Results are presented as the differences between the fixed and motion cases.

First, all hot-wires exhibit similar trends, with an energy peak that increases with the Strouhal number until reaching a maximum, followed by a decrease in the energy peak. Moreover, it appears that the maxima vary according to the hot-wire location in the wake: the hot-wires at the left and right edges of the wake (HW2 and HW4) present the lowest impact, while the upper hot-wire (HW1) shows the highest one. HW2 and HW4 signals are too weak to draw any definitive conclusions, while the central hot-wire (HW3) exhibits lower maxima for the majority of surge motion cases; therefore, HW1 is preferred for the following investigations.

Regarding the energy peaks of the HW1 PSD, the maximum energy level is reached for the $\mathbf{HW_{0.24}}$ case. This surge motion is deduced to show the greatest impact and is selected for a more detailed S-PIV analysis performed in Sect. 3.2.

3.2 Phase-averaged analysis of the most impactful surge motion using S-PIV

Observations of the wake dynamics for the aforementioned motion frequency of $St = 0.24$ ($\mathbf{SPIV_{0.24}}$) are obtained thanks to S-PIV measurements.

Figure 7 shows the phase-averaged velocity deficit fields $\widetilde{\Delta u}$ normalized by U_{hub}. The position of the porous disk is represented by the dashed-line circle, and the studied phases are $[0; \frac{\pi}{3}; \frac{2\pi}{3}; \pi; \frac{4\pi}{3}; \frac{5\pi}{3}]$, which correspond approximately to the phases

https://doi.org/10.5194/wes-2026-41
Preprint. Discussion started: 17 February 2026

eawe european academy of wind energy
Open Access WIND ENERGY SCIENCE DISCUSSIONS

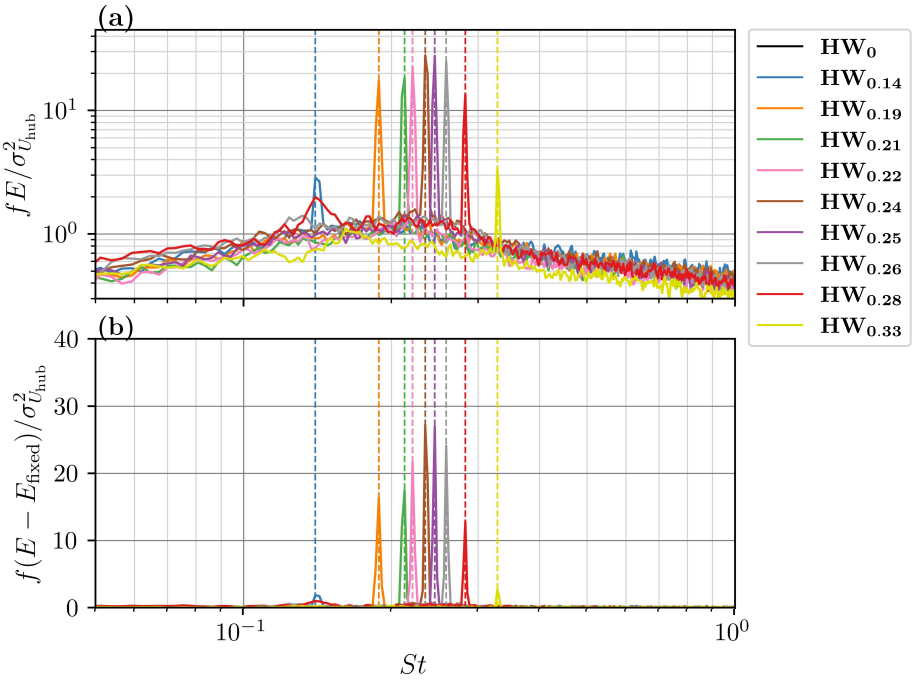

Figure 5. Normalized and premultiplied energy spectra E^* of the HW1 velocity, at $8.125D$ downstream of the disk (a), and normalized and premultiplied energy difference between the fixed and the motion cases $E^* - E^*_{\mathrm{fixed}}$ (b). The vertical dashed-lines represent the motion frequency.

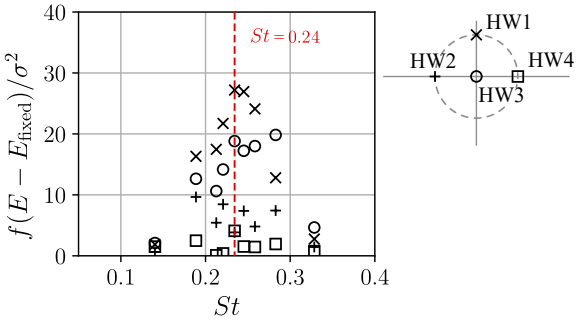

Figure 6. Normalized and premultiplied energy difference maxima $E^* - E^*_{\mathrm{fixed}}$, for the four hot-wires.

when the extrema of the wake parameters appear. Black contours and crosses represent the phase-averaged wake contours and centers, while the gray contours and crosses represent the time-averaged ones.

The observed modifications are directly attributed to the harmonic surge motion imposed on the porous disk. Indeed, in the fixed case (not shown here), the phase-averaged and time-averaged parameters coincide, indicating negligible wake modifications and the absence of periodic dynamics at that frequency.

https://doi.org/10.5194/wes-2026-41
Preprint. Discussion started: 17 February 2026

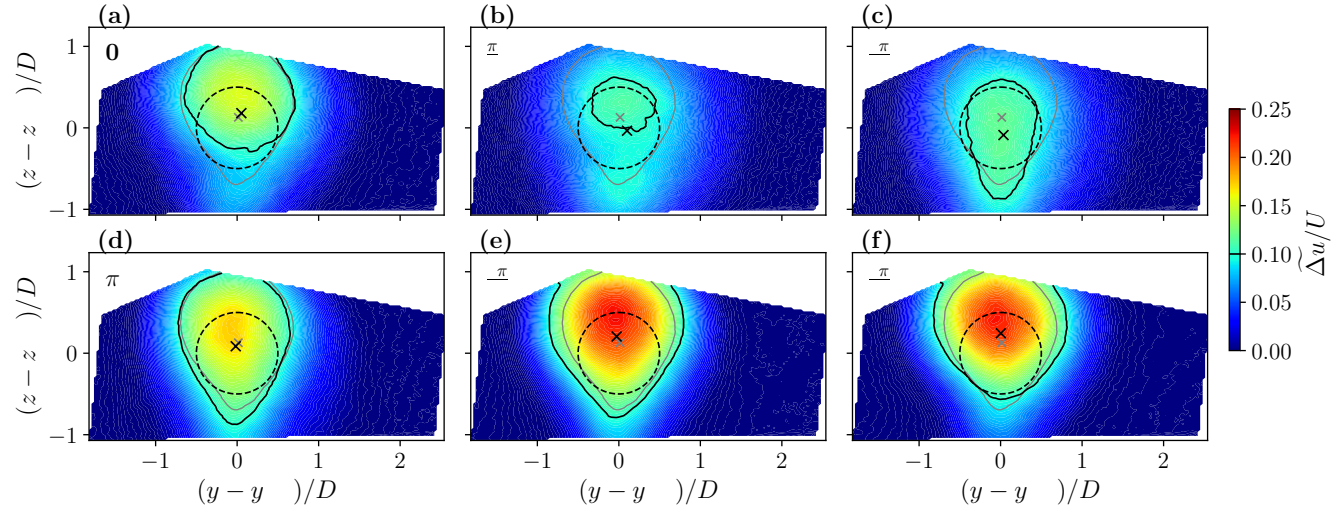

Figure 7. Phase-averaged streamwise velocity deficit fields in FFOR $\widetilde{\Delta u}$ normalized by the inlet velocity at hub height for different phases $[0; \frac{\pi}{3}; \frac{2\pi}{3}; \pi; \frac{4\pi}{3}; \frac{5\pi}{3}]$ for the $\mathbf{SPIV_{0.24}}$ case. The dashed-line circle represents the porous disk location. The black and gray contours and crosses represent the phase-averaged and time-averaged wake contour and center, respectively.

The wake undergoes large modifications, especially in the velocity deficit values, synchronized with the disk motion, with a minimum and maximum reached at phase $\frac{\pi}{3}$ **(b)** and $\frac{4\pi}{3}$ **(e)**, respectively. In addition to the variations in velocity deficit, the wake undergoes significant displacement along the phases. It reaches its lowest position at phase $\frac{2\pi}{3}$ **(c)** and its highest at phase $\frac{5\pi}{3}$ **(f)**, showing a phase shift of $\frac{\pi}{3}$ compared to the variations in velocity deficit.

It appears that the time-averaged wake center is located above the porous disk center, which differs from the fixed configuration - *c.f.* Appendix A. Moreover, the upper and lower parts of the wake are not symmetric, due to the rod wake. This is visible across all phases but is particularly evident in phases when the velocity deficit values are the lowest, at phases $\frac{\pi}{3}$ **(b)** and π **(d)**.

Figure 8 shows the phase-averaged velocity deficit fields $\widetilde{\Delta u_\mathrm{m}}$ normalized by U_hub, similar to Fig. 7, but in MFoR. The MFoR analysis allows for the observation of the wake dynamics by suppressing the crosswise displacement of the wake. The dashed-line crossing represents the wake centers for all phases.

As seen in Fig. 7, the wake contours follow a distinct evolution during the motion cycle. The wake surface is minimal at phase $\frac{\pi}{3}$, and maximal at phase $\frac{4\pi}{3}$. At the minimal wake surface, the wake exhibits an axisymmetric shape, while the impact of the rod begins to be visible for phases $\frac{2\pi}{3}$ and $\frac{5\pi}{3}$, and is maximal when the wake surface is at its maximum.

The wake surface modulation is correlated with a velocity one; high $\widetilde{\Delta u_\mathrm{m}}$ implies high $\widetilde{S_\mathrm{wk}}$ **(e, f)**, and low $\widetilde{\Delta u_\mathrm{m}}$ implies low $\widetilde{S_\mathrm{wk}}$ **(b, c)**, which is consistent with the momentum conservation law.

Figure 9 presents the phase-averaged wake center coordinates $(\widetilde{y_\mathrm{c}}, \widetilde{z_\mathrm{c}})$ **(a)**, the phase-averaged wake surface $\widetilde{S_\mathrm{wk}}$ **(b)**, and the phase-averaged available wind power in FFoR $\widetilde{P}$ and in MFoR $\widetilde{P_\mathrm{m}}$ **(c)**, as defined in Sect. 2.2.3. The colored zones represent

https://doi.org/10.5194/wes-2026-41
Preprint. Discussion started: 17 February 2026

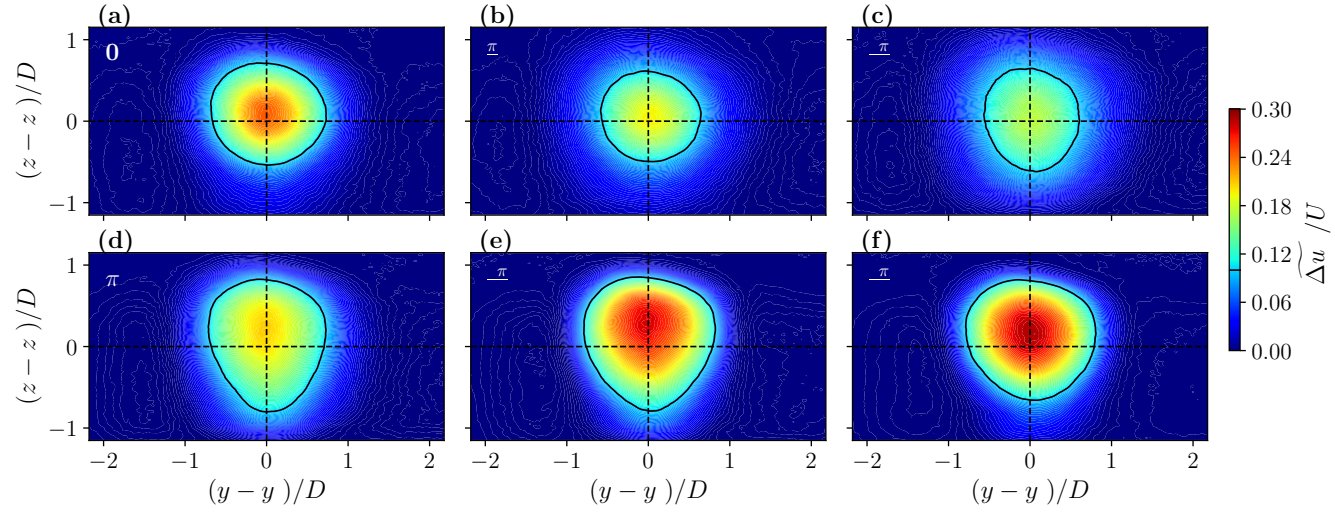

Figure 8. Phase-averaged streamwise velocity deficit fields in MFoR $\widetilde{\Delta u_{\mathrm{m}}}$ normalized by the inlet velocity at hub height for different phases, same as Fig. 7.

the statistical uncertainties defined in the previous study Hubert et al. (2024b). The uncertainties of the wake center coordinates are not visible due to their small values.

All wake parameters appear to have significant variations related to a relative sinusoidal shape. The variations of $\widetilde{y_{\mathrm{c}}}$ are less pronounced than those of $\widetilde{z_{\mathrm{c}}}$, showing peak-to-peak amplitudes of $0.15D$ and $0.35D$, respectively. $\widetilde{S_{\mathrm{wk}}}$ exhibits significant variations, with a peak-to-peak amplitude of $1.25S_{\mathrm{disk}}$. $\widetilde{P_{\mathrm{m}}}$ shows lower variations than those of $\widetilde{P}$, due to a wake displacement bias. Indeed, $\widetilde{P}$ is defined according to a fixed circle related to the fixed porous disk, without taking into account the displacements of the wake due to the motion, in contrast to $\widetilde{P_{\mathrm{m}}}$, which follows them. These variations are inversely synchronized with both $\widetilde{S_{\mathrm{wk}}}$ and $\widetilde{z_{\mathrm{c}}}$.

3.3 Analysis of the subharmonic frequency peak

As observed in Sect. 3.1, subharmonic frequency peaks are visible in the wake of the porous disk at given surge frequencies, particularly at $St = 0.28$. The aim of this subsection is to determine the underlying phenomenon related to this unexpected result, utilizing coherence and phase computations, as well as POD analysis. An experimental test with the wind on and a ballast in place of the porous disk, while maintaining an identical weight, did not show any peak, proving that the underlying phenomenon is not generated by artifacts of the experimental setup, such as vibrations.

Figure 10 shows E^* of the four hot-wire velocities, as presented in Fig. 3, for the $\mathbf{HW_0}$ and $\mathbf{HW_{0.28}}$ cases.

First, for this case, both harmonic and subharmonic signatures are visible for all hot-wires, but the subharmonic is particularly visible for HW2 and HW4, which are located at hub height to the left and right of the model, respectively. This indicates that the phenomenon is essentially confined to the lateral direction of the wake. Contrary to the harmonic frequency peaks, the

https://doi.org/10.5194/wes-2026-41
Preprint. Discussion started: 17 February 2026

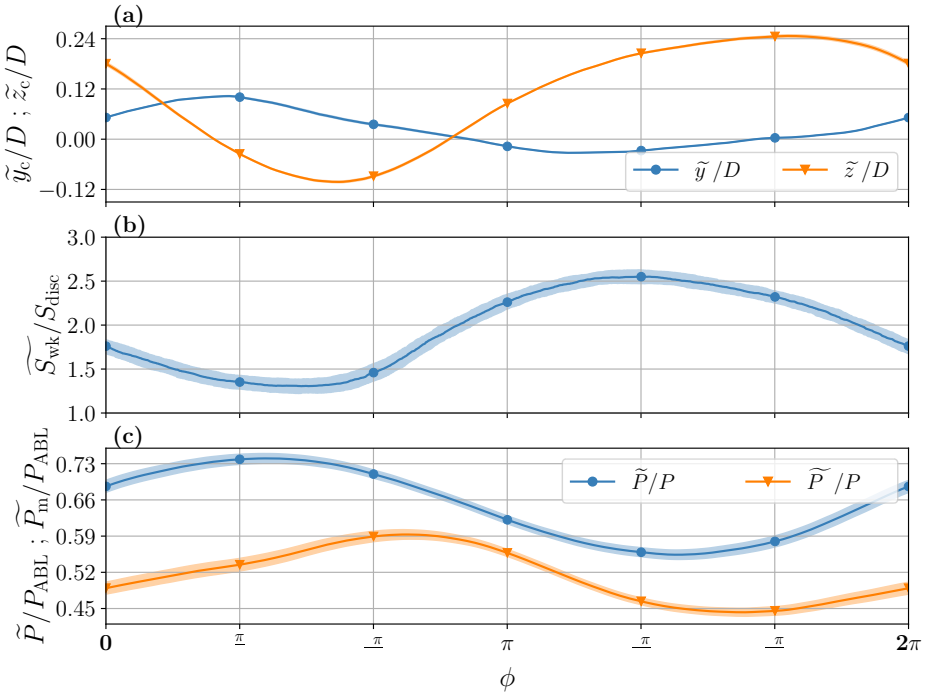

Figure 9. Phase-averaged wake center coordinates $\widetilde{y_c}$ and $\widetilde{z_c}$ normalized by D **(a)**, wake surface $\widetilde{S_{wk}}$ normalized by S_{disk} **(b)**, and available wind power in FFoR $\widetilde{P}$ and in MFoR $\widetilde{P_m}$ normalized by the available wind power present in the ABL inflow P_{ABL} **(c)**, for the $\mathbf{SPIV_{0.24}}$ case. The colored zones represent the statistical uncertainties of the phase-averaged values, defined in Hubert et al. (2024b). Each symbol corresponds to the phases shown in Fig. 7 and 8.

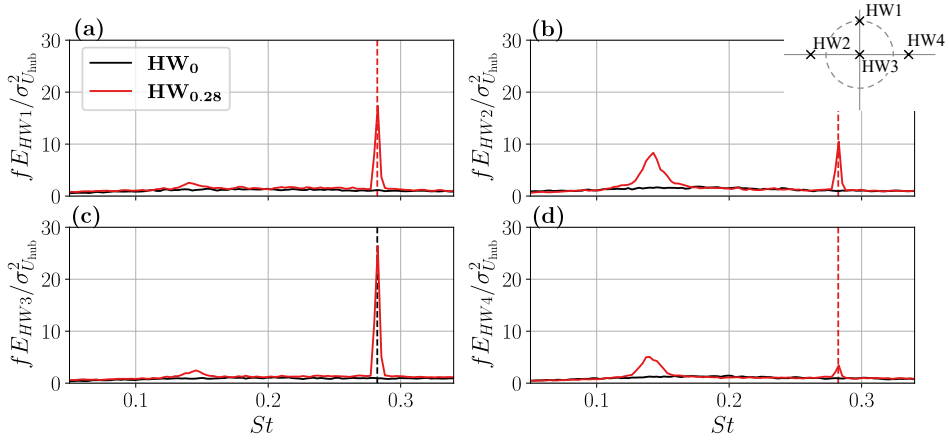

Figure 10. Normalized and premultiplied energy spectra E^* of the velocity of HW1 (a), HW2 (b), HW3 (c), and HW4 (d), for the $\mathbf{HW_0}$ and $\mathbf{HW_{0.28}}$ cases. The vertical dashed-line corresponds to the frequency of the motion case.

https://doi.org/10.5194/wes-2026-41
Preprint. Discussion started: 17 February 2026

eawe european academy of wind energy
Open Access WIND ENERGY SCIENCE DISCUSSIONS

subharmonic ones are visible over a larger frequency range with a maximum at half the motion frequency. This is representative of a pseudo-periodic phenomenon.

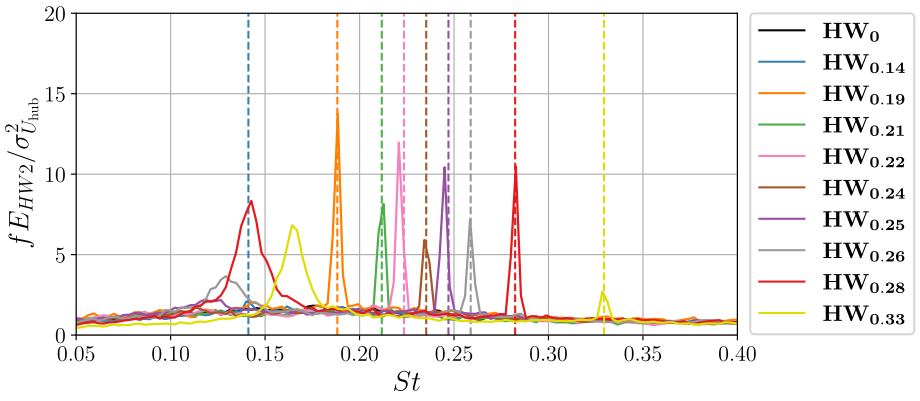

Figure 11. Normalized and premultiplied energy spectra E^* of the HW2 velocity for the hot-wire surge motion cases. The vertical dashed-lines correspond to the frequency of the motion cases.

Figure 11 shows E^* of the HW2 velocity on a linear scale, in which the subharmonic frequency peak is the strongest. It appears that the subharmonic frequency peak is visible for a certain frequency range, from $\mathbf{HW_{0.25}}$ to $\mathbf{HW_{0.33}}$, and that its maximum energy level is reached for $\mathbf{HW_{0.28}}$.

Table 3 presents the energy levels reached at the motion frequency St_{motion} and at $St_{\mathrm{motion}}/2$, along with the ratio between them. It shows that the ratio between the two energy levels decreases inversely with the Strouhal number. The fact that $E^*(St_{\mathrm{motion}})$ is higher than $E^*(St_{\mathrm{motion}}/2)$ indicates that the phenomenon related to the subharmonic frequency peak has a lower impact compared to the wake dynamics associated with the frequency motion at this position in the wake. Above $\mathbf{HW_{0.28}}$, the trend is reversed; $\mathbf{HW_{0.33}}$ presents an energy ratio higher than 1.

Table 3. Normalized and premultiplied energy maxima of the HW2 velocity for the harmonic frequency peak $E^*(St_{motion})$, related to the motion frequency, and the subharmonic frequency peak $E^*(St_{motion}/2)$.

Case	$E^*(St_{\mathrm{motion}})$	$E^*(St_{\mathrm{motion}}/2)$	$\frac{E^*(St_{\mathrm{motion}}/2)}{E^*(St_{\mathrm{motion}})}$
$\mathbf{HW_{0.25}}$	10.4	2.2	0.21
$\mathbf{HW_{0.26}}$	7.2	3.7	0.51
$\mathbf{HW_{0.28}}$	10.5	8.3	0.80
$\mathbf{HW_{0.33}}$	2.7	6.8	2.53

In the subsequent subsections, three cases are compared: $St = 0.28$, where the secondary peak is maximum; $St = 0.14$, where it is not visible; and the no-motion case for reference.

https://doi.org/10.5194/wes-2026-41
Preprint. Discussion started: 17 February 2026

eawe european academy of wind energy
Open Access WIND ENERGY SCIENCE DISCUSSIONS

3.3.1 Coherence and phase analysis

Figure 12 exhibits the coherence functions $\mathcal{C}_{i,j}$ and phases $\mathcal{P}_{i,j}$ between the six hot-wire pairs (i,j) for the three cases (no-motion, $St = 0.14$ and $St = 0.28$). The results show similar trends, with the majority of the hot-wire pairs exhibiting a slight coherence value at low Strouhal numbers. For $\mathcal{C}_{1,3}$ **(b)**, this can sustain up to about $St = 0.1$ with associated phases of 0, indicating that HW1 and HW3 signals are in phase; whereas for $\mathcal{C}_{2,4}$, the coherence value is ≈ 0.11 in the range $St = 0.02$ to 0.22, with associated phases of $\pm\pi$, indicating that HW2 and HW4 signals are in phase opposition.

Concerning the motion cases ($\mathbf{HW_{0.14}}$ and $\mathbf{HW_{0.28}}$), the harmonic frequency peak is visible for all hot-wire pairs, except for $\mathcal{C}_{2,4}$ for $\mathbf{HW_{0.14}}$ for which it might be hidden by the noise. Their associated phases are approximately 0, meaning that all hot-wires are in phase and that their velocity variations caused by the porous disk motion occur synchronously.

Regarding $\mathbf{HW_{0.28}}$, the subharmonic frequency peak is also visible for all hot-wire pairs, except for $\mathcal{C}_{1,3}$. $\mathcal{C}_{2,4}$ is particularly significant compared to the others, reaching almost 0.4 **(i)**. This shows that the phenomenon related to the subharmonic frequency peak is essentially confined in the lateral direction, as observed in Fig. 10. Moreover, knowing that HW2 and HW4 signals are in phase opposition **(k)**, the phenomenon is anti-correlated between the right and left sides of the wake.

Figure 13 presents a zoom on the $(2,4)$ hot-wire pair, where the coherence functions and phases of the $\mathbf{HW_0}$, $\mathbf{HW_{0.25}}$, $\mathbf{HW_{0.26}}$, $\mathbf{HW_{0.28}}$, and $\mathbf{HW_{0.33}}$ cases are plotted - *i.e.* the cases for which a subharmonic frequency peak is visible (Fig. 11), plus the fixed case. As observed in Fig. 12, the results show that the peaks at the motion frequency are associated with a phase close to 0, and the peaks at the subharmonic frequency have a phase of $\pm\pi$, confirming the alternative nature of the dynamics for all cases showing this phenomenon.

3.3.2 Proper orthogonal decomposition analysis

In this subsection, POD calculation is performed on the velocity deficit fields of the $\mathbf{SPIV_0}$, $\mathbf{SPIV_{0.14}}$, and $\mathbf{SPIV_{0.28}}$ cases, with the objective of comparing the most energetic spatiotemporal modes according to the studied cases.

Figure 14 shows the amplitudes of the modes for the $\mathbf{SPIV_0}$, $\mathbf{SPIV_{0.14}}$, and $\mathbf{SPIV_{0.28}}$ cases. Knowing that σ_i represents the contribution of the mode i to the total TKE, the mode 0 has the highest contribution to the total turbulent kinetic energy (TKE) of the wake with an amplitude of about 6% for the three cases. It corresponds to the time-averaged velocity deficit fields and is not presented here. As observed in several previous studies for a fixed wind turbine wake (Bastine et al., 2014; De Cillis et al., 2020), the curves show a slow decrease in the mode contribution to the total energy. While they present approximately the same trends, some differences are visible between $\mathbf{SPIV_{0.28}}$ and the other two cases. Indeed, $\mathbf{SPIV_{0.28}}$ case presents higher amplitudes, especially for modes 3 and 4 **(b)**.

Figures 15 and 16 exhibit the streamwise, lateral, and vertical components of the spatial modes χ_1 and χ_2, respectively. The results of the $\mathbf{SPIV_0}$ case are in accordance with previous works for a fixed wind turbine wake - *e.g.* Andersen et al. (2013); Bastine et al. (2014); Geibel and Bangga (2022) - with clear dipole structures rotated by 90° to each other (Fig. 15 and 16 **(a, d, g)**), distinct central regions (Fig. 15 **(b, e, h)** and Fig. 16 **(c, f, i)**), and quadripole structures (Fig. 15 **(c, f, i)** and Fig. 16 **(b,**

https://doi.org/10.5194/wes-2026-41
Preprint. Discussion started: 17 February 2026

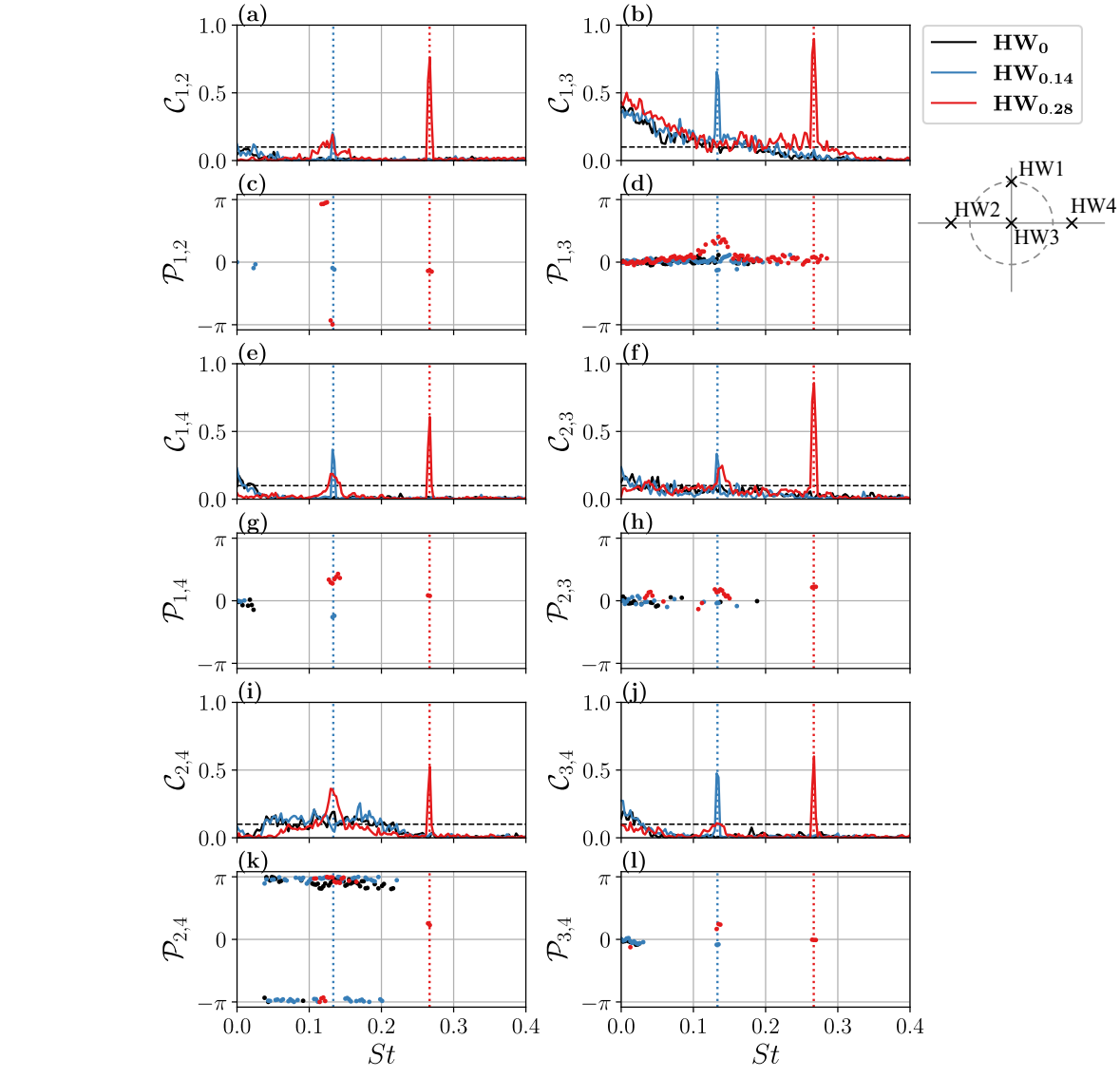

Figure 12. Coherence functions $\mathcal{C}_{i,j}$ **(a, b, e, f, i, j)** and phases $\mathcal{P}_{i,j}$ **(c, d, g, h, k, l)** between the four hot-wires for the $\mathbf{HW_0}$, $\mathbf{HW_{0.14}}$, and $\mathbf{HW_{0.28}}$ cases. The horizontal dashed-line is the threshold value $\mathcal{C}_{i,j} = 0.1$ above which the two hot-wires show a non-negligible correlation, and therefore for which the phase is plotted. The vertical dotted blue and red lines represent the motion frequencies.

335 **e, h)**). Thus, the first mode is associated with lateral wake meandering and the second mode is associated with vertical wake meandering.

Case $\mathbf{SPIV_{0.14}}$ does not significantly impact spatial modes χ_1 and χ_2, in accordance with the findings of Raibaudo et al. (2023). On the contrary, spatial modes in case $\mathbf{SPIV_{0.28}}$ show some discrepancies compared to the two other cases; the dipole

https://doi.org/10.5194/wes-2026-41
Preprint. Discussion started: 17 February 2026

eawe european academy of wind energy
Open Access WIND ENERGY SCIENCE DISCUSSIONS

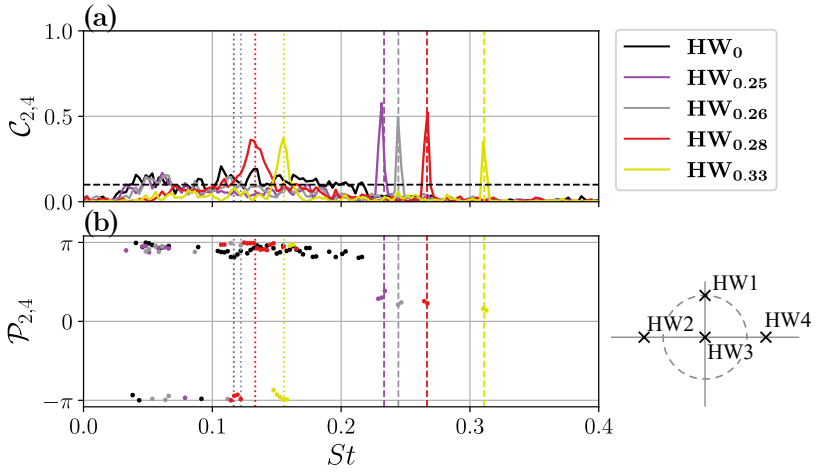

Figure 13. Coherence functions $\mathcal{C}_{i,j}$ **(a)** and phases $\mathcal{P}_{i,j}$ **(b)** between HW2 and HW4 for the $\mathbf{HW_0}$, $\mathbf{HW_{0.25}}$, $\mathbf{HW_{0.26}}$, $\mathbf{HW_{0.28}}$, and $\mathbf{HW_{0.33}}$ cases. The horizontal dashed-line is the threshold value $C_{i,j} = 0.1$ above which the two hot-wires show a non-negligible correlation, and therefore for which the phase is plotted. The vertical dashed-lines represent the motion frequencies, and the vertical dotted lines represent the half motion frequencies.

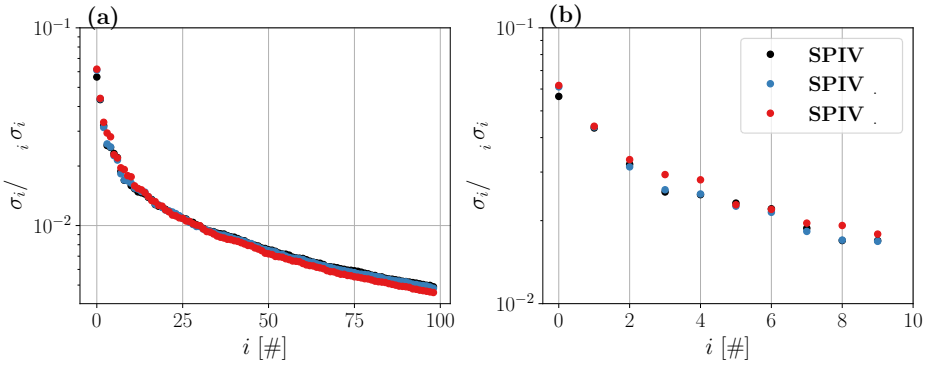

Figure 14. Amplitudes σ_i of the modes i, normalized by the total amplitude of the POD (TKE), for the $\mathbf{SPIV_0}$, $\mathbf{SPIV_{0.14}}$, and $\mathbf{SPIV_{0.28}}$ cases **(a)**, and a zoom on the 10 first modes **(b)**.

of the first mode appears to be at a higher vertical position (Fig. 15 **(c)**), and the dipole of the second mode is less noticeable,
340 caused by a broader negative bottom zone in the streamwise direction (Fig. 16 **(g)**).

Figure 17 exhibits the normalized and premultiplied energy spectra of the temporal modes associated with the previously mentioned spatial modes χ_1 and χ_2 (Fig. 15 and 16, respectively). The results show that both harmonic and subharmonic frequencies have a signature in the first two modes. However, the second mode is preferably related to the motion, with a high energy frequency peak at the Strouhal number motion **(b)**, while the first mode is mainly related to the subharmonic frequency

https://doi.org/10.5194/wes-2026-41
Preprint. Discussion started: 17 February 2026

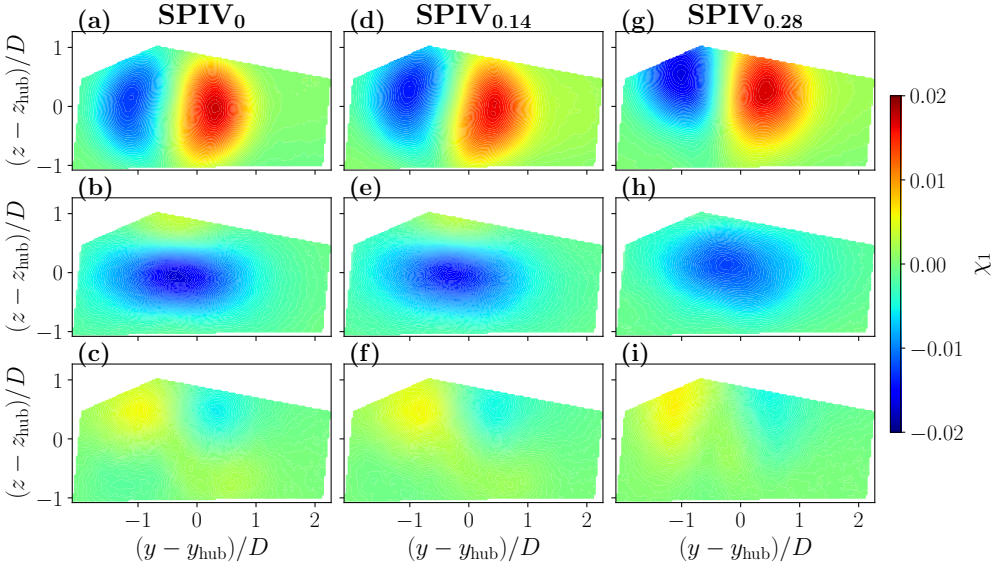

Figure 15. Spatial mode χ_1 in the streamwise (first row), lateral (second row), and vertical (third row) directions for the **SPIV$_0$ (a - c)**, **SPIV$_{0.14}$ (d - f)**, and **SPIV$_{0.28}$ (g - i)** cases.

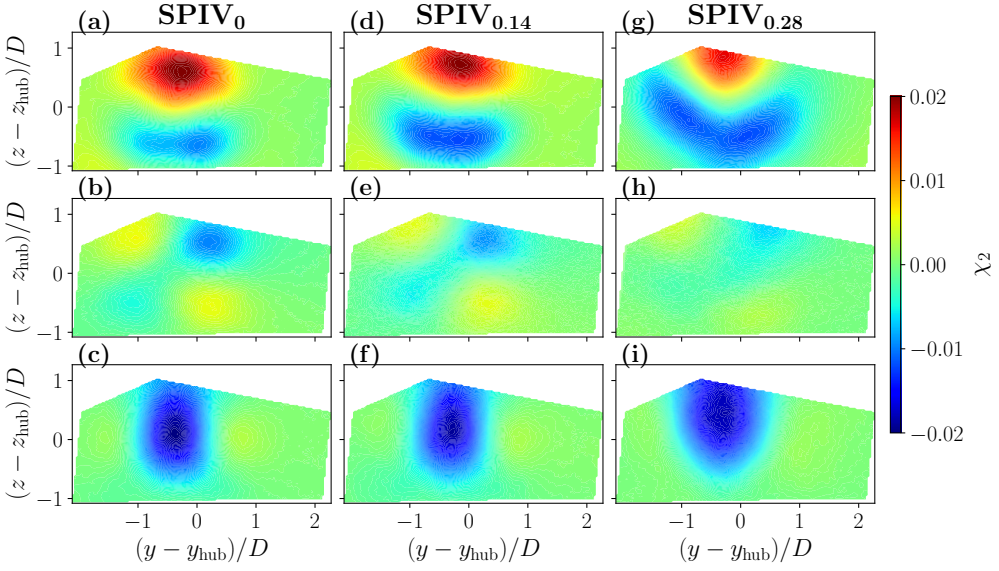

Figure 16. Spatial mode χ_2, same as Fig. 15.

345 peak **(a)**. Considering that the first mode is associated with a lateral displacement of the wake, the subharmonic frequency peak seems to be related to a lateral wake meandering, which is consistent with the previous findings presented in Fig. 10 and 12.

https://doi.org/10.5194/wes-2026-41
Preprint. Discussion started: 17 February 2026

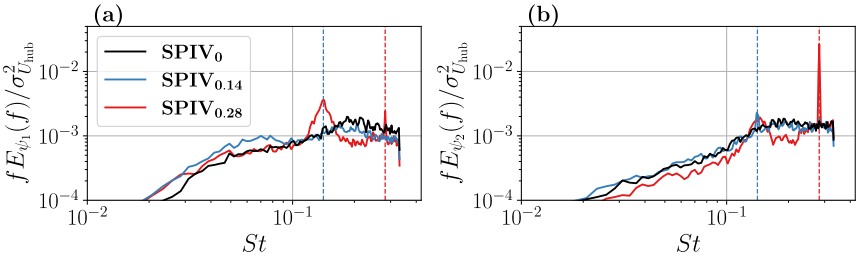

Figure 17. Normalized and premultiplied energy spectra of the temporal modes in the streamwise direction ψ_1 **(a)** and ψ_2 **(b)**, for the $\mathbf{SPIV_0}$, $\mathbf{SPIV_{0.14}}$, and $\mathbf{SPIV_{0.28}}$ cases. The vertical dashed-lines represent the Strouhal number of the associated motions.

The modes 3 and 4 are presented in Appendix B. The spatial modes χ_3, χ_4 present no significant differences between the cases and are similar to previous works with quadripole structures in the streamwise direction - *e.g.* Andersen et al. (2013). Moreover, the associated temporal modes ψ_3, ψ_4 do not exhibit significant subharmonic frequency peaks.

4 Discussion

Most impactful surge frequency

At $8.125D$ downstream of the turbine model, the most impactful surge motion frequency is found for a Strouhal number of $St = 0.24$ ($\mathbf{HW_{0.24}}$). This result is coherent with those of Li et al. (2022), who showed through numerical simulations, supported by a linear stability analysis, that sway and roll motions with similar amplitudes amplified the far wake meandering in the range $St = 0.2 - 0.6$, with a peak response observed at $St = 0.2$ and $St = 0.3$, respectively. At $4.6D$ downstream, Schliffke et al. (2024) showed that surge motions of similar amplitudes have a higher signature with $St = 0.35$ than with $St = 0.25$. Although based on wake recovery, a steady metric compared to spectral response, Messmer et al. (2024) showed that surge and sway motions exhibit maximal wake recovery at about $St \approx [0.4 - 0.5]$ in the far wake of a reduced-scale turbine. Considering the differences in the studies (motion type and amplitude, methods), the most impactful motion frequency found in the present work falls within the range of values reported in the literature.

S-PIV results and wake dynamics

The position of the time-averaged wake is located above the disk center (Fig. 7), whereas the one for the fixed case is located slightly below, as expected in a positive shear flow or with the influence of the rod. Additionally, this feature was not detected in the previous study performed by Hubert et al. (2024b) in a higher sheared inflow and a surge motion frequency of $St = 0.11$ or by Barile et al. (2026) through LES simulations of an actuator disc in a similar flow for a surge motion frequency range of $St = 0.1 - 0.5$. The present configuration (lower shear and most impactful Strouhal number) is more prone to highlight the dynamics modifications generated by the surge motion on the wake, which are characterized, among others, by a wake center fluctuation mainly above the disk center. This result can be correlated with the findings reported in Sect. 3.1 and in Schliffke

https://doi.org/10.5194/wes-2026-41
Preprint. Discussion started: 17 February 2026

eawe european academy of wind energy
Open Access WIND ENERGY SCIENCE DISCUSSIONS

et al. (2024), where the highest signature values were systematically observed at a location situated above the disk center ($HW1$). Furthermore, Barile et al. (2026) observed a similar behavior, i.e. a progressive vertical shift of the surge-generated structures, and so of the location of the maxima of fluctuations, appears with the downstream distance,should the inflow be non-uniform. Nevertheless, this result needs to be further investigated to understand the physical phenomena at play.

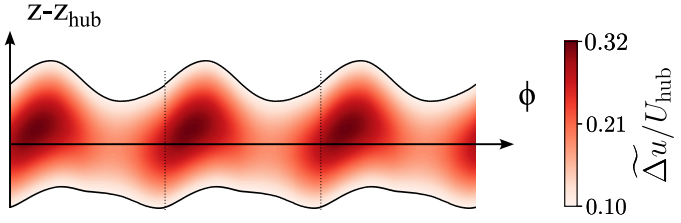

Figure 18. Schematic view of the surge motion impact on the far wake of a floating wind turbine, based on the phase-averaged results.

Figure 18 presents a schematic view of the observed impact of surge motion on the far wake of a FOWT, with modifications to the wake surface and velocity deficit on the same order of magnitude as those found in the experiments of $\mathbf{SPIV_{0.24}}$. With this configuration, the surge motion induces high velocity deficit variations in the far wake of the porous disk. It imposes wake modulation, with an extension and contraction of the wake surface in phase opposition to the velocity deficit variations. The results present similarities with a previous work performed in the same facility for the surge motion case with realistic amplitude and frequency (Hubert et al., 2024b); as in the aforementioned study, the surge motion imposes a modulation of $\widetilde{S_{\text{wk}}}$ and $\widetilde{P_{\text{m}}}$ in phase opposition, in agreement with momentum conservation. This modulation was also observed in the range $St = [0.5, 0.9]$ in the studies of Duan et al. (2022) and Messmer et al. (2024) performed in lower turbulence inflow conditions. However, the present velocity deficit contours are inclined at a positive angle that induces an artificial vertical variation of the wake center location. This feature was not observed in previous studies and will be discussed in the following sections.

Quasi-steady state analysis

Considering the low frequencies of the investigated motions compared to the wake scale ($St < 0.5$), the results are compared to engineering steady wake model predictions to evaluate whether the observed wake modifications can be considered as quasi-steady - *i.e.* the result of a succession of steady states rather than dynamic processes.

At the wake center of the $\mathbf{SPIV_{0.24}}$ surge case, $\widetilde{u_{\text{m}}}$ undergoes an amplitude variation of $\pm 0.17 U_{\text{hub}}$, while the motion of the porous disk induces a streamwise velocity variation of $0.31 U_{\text{hub}}$ in the near wake. Following the wake model proposed by Bastankhah and Porté-Agel (2014), this theoretically implies a velocity difference lower than $0.01 U_{\text{hub}}$, at $x = 8.125D$ downstream of the porous disk. This theoretical value is much lower than the observed one, indicating that the perturbation created by the motion cannot be assimilated to a succession of steady states, and that the perturbation caused by the disk motion appears to be amplified within the wake.

Inclined surge-generated coherent structures

https://doi.org/10.5194/wes-2026-41
Preprint. Discussion started: 17 February 2026

eawe european academy of wind energy
Open Access WIND ENERGY SCIENCE DISCUSSIONS

The large vertical far wake translations, seen in this surge case (Fig. 9 **(a)**), are induced by a side effect, that is the shear present in the inflow, advecting the turbulent structures created by the disk at different velocities, as seen for tip vortices in the presence of shear (see Lu and Porté-Agel (2011); Kleusberg et al. (2019)). The porous disk subjected to surge motion induces coherent structures in its wake (Duan et al., 2022; Messmer et al., 2024), the shear present in the ABL might delay the bottom part of the surge wake dynamics compared to that of the top and induces the inclined velocity deficit patterns seen in Fig. 18.

To check the validity of this hypothesis, an estimation of the phase delay that the surge-generated structures would have at $x = 8.125D$ downstream of the porous disk is performed, using the assumption that the flow structures contained in the wake are passively transported in the atmospheric flow, governed by an advection velocity U_{a}. According to Hubert et al. (2024a), the advection velocity in case of surge motion is about $U_{\mathrm{a}} = 0.8U_{\mathrm{hub}}$. Knowing that the inflow velocity differences between the top and bottom disk edges are about $0.03U_{\mathrm{hub}}$ (Fig. 2), the advection velocities are $0.79U_{\mathrm{hub}}$ and $0.83U_{\mathrm{hub}}$ at the top and the bottom, respectively. These values correspond to phase delays of 0.63 rad, at $8.125D$ downstream of the porous disk.

The phase delay between the highest position of the wake top edge and the lowest position of the wake bottom edge (schematic view in Fig. 18) is assessed to be 0.9 rad. The difference between the estimated and the observed values is not negligible, but the theoretical value is highly sensitive to the inflow velocity, which might be misestimated. Future investigations are necessary to validate this hypothesis and to provide more precise results.

Nevertheless, the observed large vertical far wake translations can be assimilated to a vertical harmonic wake meandering at the surge frequency. It explains why the POD mode associated with the vertical meandering χ_2 presents a significant peak of energy at the surge frequency.

Subharmonic frequency peak

The phenomenon underlying the subharmonic frequency peak, observed in wakes under surge motions with $St > 0.25$, appears to be essentially confined in the lateral direction (Fig. 10 and Fig. 15). The left and right edges of the wake undergo velocity variations in phase opposition (Fig. 12), demonstrating that the phenomenon occurs alternately rather than simultaneously. Duan et al. (2022) showed that surge motions (with equivalent amplitudes and $St = 0.55$) induce periodic vortex rings in the near wake, which are no longer visible after $6D$ but are replaced by a regular wake swinging. The findings of the present article are consistent with those observations, and the subharmonic frequency peak can be associated with a far wake meandering, characterized by large-scale translations of the wake, at a frequency range rather than at a specific frequency (Fig. 10). The fact that this subharmonic frequency peak is not visible in the energy spectra of surge motions with $St < 0.25$ might be attributed to the lower receptivity of the wake to this Strouhal number range, but also to the relatively higher energy present in the inflow.

This phenomenon should not be confused with the broad-band wake meandering caused by the large-scale turbulent structures present in the ABL. Here, both sources of meandering coexist in the far wake of the porous disk.

https://doi.org/10.5194/wes-2026-41
Preprint. Discussion started: 17 February 2026

eawe european academy of wind energy
Open Access WIND ENERGY SCIENCE DISCUSSIONS

5 Conclusions

This article aims to describe the far wake behavior of a floating wind turbine in the context of surge motions. Thus, experiments are performed $8.125D$ downstream of a porous disk, installed in the ABL wind tunnel of the LHEEA. The porous disk is positioned in the upper part of a 1:500 neutral marine ABL, with low shear and limited ground effect, facilitating the wake dynamic observations, and is subjected to harmonic surge motions at different Strouhal numbers. Several observations have been made:

- Hot-wire measurements are performed to identify the Strouhal number at which the surge motion has the greatest impact on the far wake of the turbine model. The impacts are estimated with the energy levels reached by the frequency peak associated with the motion in the wake velocity spectra of the hot-wire signals. The results show an energy peak increase until a maximum and a decrease, exhibiting a critical Strouhal number of $St = 0.24$, which aligns with previous results (Li et al., 2022; Messmer et al., 2024).

- The far wake dynamics of the porous disk subjected to surge motion at this critical Strouhal number are investigated using an S-PIV system, which employs two frames of reference (the FFoR and the MFoR) and a phase-averaging with kernel smoothing algorithm. It appears that surge motion leads to the contraction and the expansion of the wake surface in the crosswise plane, and modifies the available wind power within the wake. Inclined periodic coherent structures are induced by the surge motion in the far wake, leading to high variations of the vertical wake position that cause vertical wake meandering. The results show that wake crosswise surface and velocity modulations are in phase opposition: a large wake surface implies high velocity deficit (thus, a low velocity), and vice-versa, consistent with momentum conservation. Moreover, a quasi-steady-state analysis is performed, indicating that the surge motion impacts are amplified in the wake.

- The reason of the inclination of the periodic coherent structures generated in the far wake is investigated using previous advection study results (Hubert et al., 2024a). The analysis indicates that the shear present in the inflow - *i.e.* velocity difference between the upper and lower edges of the disk - could lead to phase shifts similar to those seen in the experiments. This suggests that the coherent structures generated in the wake of a disk subjected to surge motion are elongated by the shear present in the ABL, resulting in the observed phenomenon. This is consistent with previous studies of tip vortices in sheared flows, indicating different travel times between the top and bottom parts of the wake - *e.g.* Lu and Porté-Agel (2011); Kleusberg et al. (2019).

- An unexpected energy peak is observed at the subharmonic frequency in the spectrum of the velocities in the far wake of the porous disk subjected to surge motion cases with $St > 0.25$. It appears to be pseudo-periodic, with a maximum reached at half the motion frequency. POD and coherence calculations are performed, showing that the phenomenon behind this subharmonic frequency peak is essentially confined in the lateral direction, with left and right velocity variations in phase opposition. Thus, the far wake appears to meander in the lateral direction, as previously observed by Duan et al. (2022) for similar motions, adding up with the meandering induced by large-scale turbulent structures present in the inflow.

https://doi.org/10.5194/wes-2026-41
Preprint. Discussion started: 17 February 2026

eawe european academy of wind energy
Open Access WIND ENERGY SCIENCE DISCUSSIONS

One main limitation in the present study is the use of a porous disk instead of a rotating turbine model. This approach simplifies the study by focusing on the far wake response to external disturbances, but a comparison between both model types involved in similar atmospheric and floating motion conditions is needed to be fully confident in the conclusions drawn.

Moreover, several hypotheses drawn in this article require deeper investigations. Indeed, the inclined periodic coherent structures are assumed to be due to the velocity difference between the upper and lower parts of the porous disk subjected to the shear flow. Similar experiments with varying shear could be performed, looking for a correlation between the inflow velocity difference and the resulting inclination of the coherent structures. Also, the meandering at a subharmonic frequency peak for some surge Strouhal numbers could be investigated using coherence and correlation functions between velocity measurements at points located upwind and downwind of the disk, similar to the approach used by Muller et al. (2015).

Appendix A: Time-averaged velocity fields

Figure A1 shows the time-averaged normalized streamwise velocity deficit fields for the $\mathbf{SPIV_0}$, and $\mathbf{SPIV_{0.24}}$ cases.

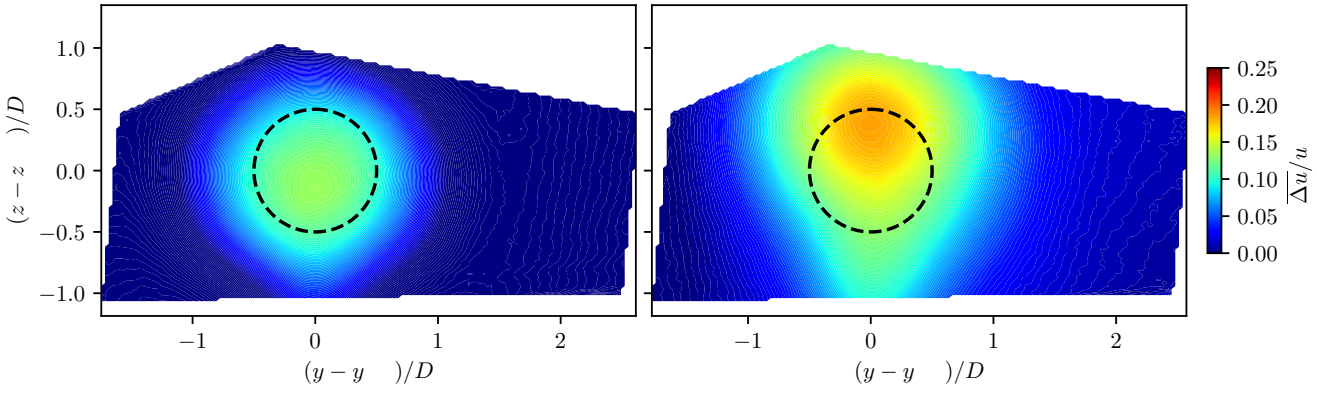

Figure A1. Time-averaged streamwise velocity deficit fields in FFOR normalized by the inlet velocity at hub height, for the $\mathbf{SPIV_0}$ (a) and $\mathbf{SPIV_{0.24}}$ (b) cases. The dashed-line circle represents the porous disk location. The black contours and crosses represent the time-averaged wake contours and centers, respectively.

Appendix B: Proper orthogonal decomposition analysis

Figures B1 and B2 show the streamwise, lateral, and vertical spatial modes χ_3 and χ_4, respectively, for the $\mathbf{SPIV_0}$, $\mathbf{SPIV_{0.14}}$, and $\mathbf{SPIV_{0.28}}$ cases.

Figure B3 shows the normalized and premultiplied energy spectra of the temporal modes ψ_3 and ψ_4 in the streamwise directions associated to the previously mentioned spatial modes.

https://doi.org/10.5194/wes-2026-41
Preprint. Discussion started: 17 February 2026

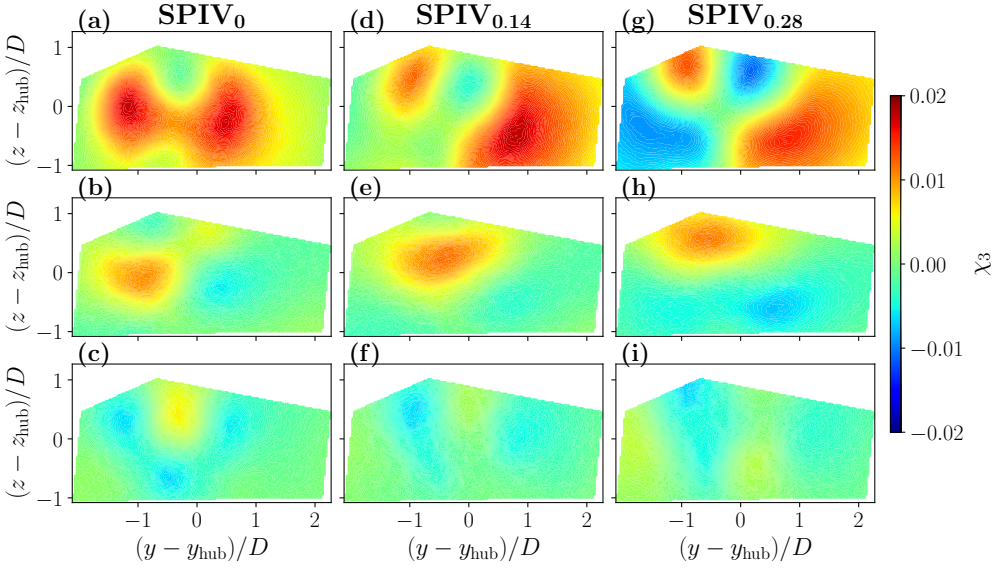

Figure B1. Spatial mode χ_3 in the streamwise (first row), lateral (second row), and vertical (third row) directions for the $\mathbf{SPIV_0}$ **(a - c)**, $\mathbf{SPIV_{0.14}}$ **(d - f)**, and $\mathbf{SPIV_{0.28}}$ **(g - i)** cases.

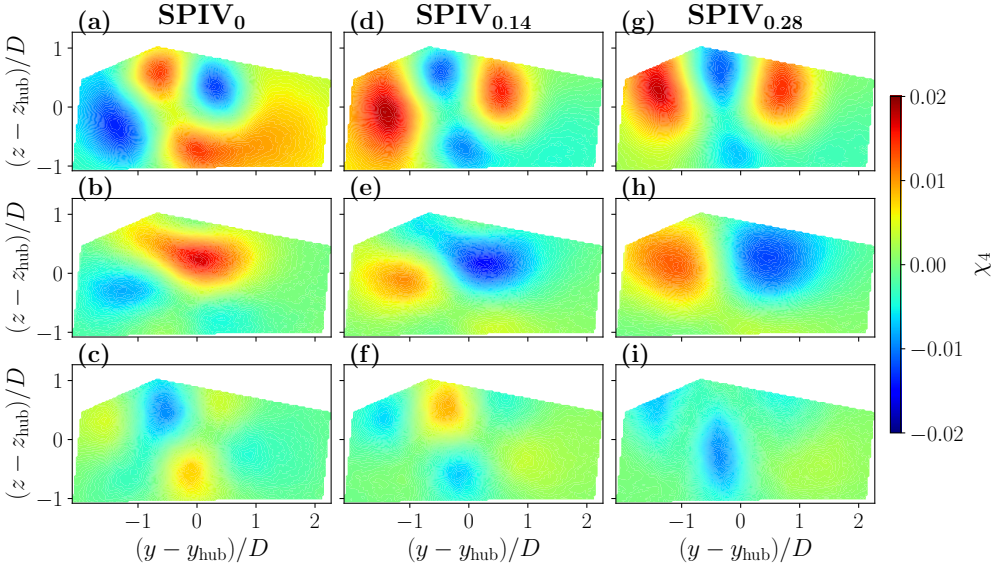

Figure B2. Spatial mode χ_4 in the streamwise (first row), lateral (second row), and vertical (third row) directions for the $\mathbf{SPIV_0}$ **(a - c)**, $\mathbf{SPIV_{0.14}}$ **(d - f)**, and $\mathbf{SPIV_{0.28}}$ **(g - i)** cases.

Data Availability. The raw data of each final figure will be available on an open research repository.

https://doi.org/10.5194/wes-2026-41
Preprint. Discussion started: 17 February 2026

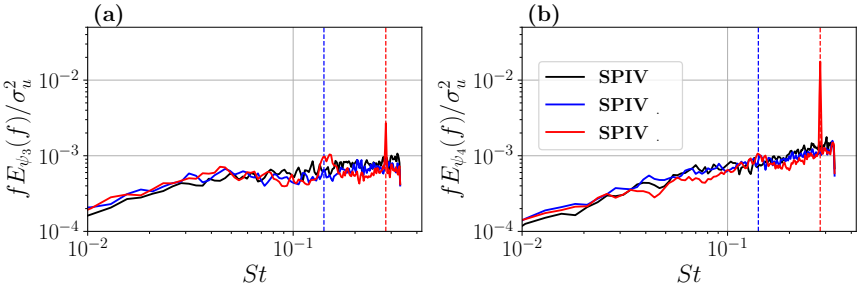

Figure B3. Normalized and premultiplied energy spectra of the temporal modes in the streamwise direction ψ_3 **(a)** and ψ_4 **(b)**, for the $\mathbf{SPIV_0}$, $\mathbf{SPIV_{0.14}}$, and $\mathbf{SPIV_{0.28}}$ cases. The vertical dashed-lines represent the Strouhal number of the associated motions.

Author Contribution. AH designed, performed the experiments, coded the postprocessing methodology, processed and analyzed the data under the supervision of and in discussion with BC and SA. SA was responsible for funding acquisition and project administration. The original draft was written by AH and reviewed and edited by SA and BC.

Competing Interests. One of the co-authors is a member of the editorial board of the journal Wind Energy Science.

Acknowledgements. This work was carried out within the framework of the WEAMEC, West Atlantic Marine Energy Community, and with funding from the Pays de la Loire Region and the École Centrale de Nantes. The authors wish to acknowledge Titouan Olivier-Martin for helping with the installation of the wind tunnel experimental setup. Additionally, large credit to Thibaud Piquet for his impressive support in getting the S-PIV system operational despite the many twists and turns.

https://doi.org/10.5194/wes-2026-41
Preprint. Discussion started: 17 February 2026

eawe european academy of wind energy
Open Access WIND ENERGY SCIENCE DISCUSSIONS

References

Adrian, R. J. and Westerweel, J.: Particle Image Velocimetry, no. 30 in Cambridge Aerospace Series, Cambridge University Press, 2011.

Ainslie, J.: Calculating the Flowfield in the Wake of Wind Turbines, Journal of Wind Engineering and Industrial Aerodynamics, 27, 213–224, https://doi.org/10.1016/0167-6105(88)90037-2, 1988.

Andersen, S. J., Sørensen, J. N., and Mikkelsen, R.: Simulation of the Inherent Turbulence and Wake Interaction inside an Infinitely Long Row of Wind Turbines, Journal of Turbulence, 14, 1–24, https://doi.org/10.1080/14685248.2013.796085, 2013.

Aubrun, S., Bastankhah, M., Cal, R., Conan, B., Hearst, R., Hoek, D., Hölling, M., Huang, M., Hur, C., Karlsen, B., Neunaber, I., Obligado, M., Peinke, J., Percin, M., Saetran, L., Schito, P., Schliffke, B., Sims-Williams, D., Uzol, O., Vinnes, M., and Zasso, A.: Round-Robin Tests of Porous Disc Models, Journal of Physics: Conference Series, 1256, 012 004, https://doi.org/10.1088/1742-6596/1256/1/012004, 2019.

Barile, D., Sosa, R.and Aubrun, S., and Otero, A.: Influence of the inflow conditions on the dynamics of a floating wind turbine wake under harmonic surge motion, to be submitted to Wind Energy Science, XX, XX, https://doi.org/XX, 2026.

Bastankhah, M. and Porté-Agel, F.: A New Analytical Model for Wind-Turbine Wakes, Renewable Energy, 70, 116–123, https://doi.org/10.1016/j.renene.2014.01.002, 2014.

Bastine, D., Witha, B., Wächter, M., and Peinke, J.: POD Analysis of a Wind Turbine Wake in a Turbulent Atmospheric Boundary Layer, Journal of Physics: Conference Series, 524, 012 153, https://doi.org/10.1088/1742-6596/524/1/012153, 2014.

Bayati, I., Bernini, L., Zanotti, A., Belloli, M., and Zasso, A.: Experimental Investigation of the Unsteady Aerodynamics of FOWT through PIV and Hot-Wire Wake Measurements, Journal of Physics: Conference Series, 1037, 052 024, https://doi.org/10.1088/1742-6596/1037/5/052024, 2018.

Belvasi, N., Conan, B., Schliffke, B., Perret, L., Desmond, C., Murphy, J., and Aubrun, S.: Far-Wake Meandering of a Wind Turbine Model with Imposed Motions: An Experimental S-PIV Analysis, Energies, 15, 7757, https://doi.org/10.3390/en15207757, 2022.

Chamorro, L. P., Arndt, R., and Sotiropoulos, F.: Reynolds Number Dependence of Turbulence Statistics in the Wake of Wind Turbines, Wind Energy, 15, 733–742, https://doi.org/10.1002/we.501, 2012.

Costanzo, G., Brindley, G., and Tardieu, P.: Wind Energy in Europe - 2024 Statistics and the Outlook for 2025-2030, Tech. rep., WindEurope, 2025.

Counihan, J.: Adiabatic Atmospheric Boundary Layers: A Review and Analysis of Data from the Period 1880–1972, 1975.

Dalla Longa, F., Kober, T., Badger, J., Volker, P., Hoyer-Klick, C., Hidalgo, I., Medarac, H., Nijs, W., Politis, S., Tarvydas, D., and Zucker, A.: Wind potentials for EU and neighbouring countries: Input datasets for the JRC-EU-TIMES Model, 2018.

De Cillis, G., Cherubini, S., Semerano, O., Leonardi, S., and De Palma, P.: POD-based Analysis of a Wind Turbine Wake under the Influence of Tower and Nacelle, Wind Energy, 24, 609–633, https://doi.org/10.1002/we.2592, 2020.

Duan, L., Sun, Q., He, Z., and Li, G.: Wake Topology and Energy Recovery in Floating Horizontal-Axis Wind Turbines with Harmonic Surge Motion, Energy, 260, 124 907, https://doi.org/10.1016/j.energy.2022.124907, 2022.

Dynamics, D.: MiniCTA Anemometer Package - How to Get Started, 2004.

ESDU: Part II: Single Point Data for Strong Winds (Neutral Atmosphere), Tech. Rep. 85020, ESDU International, 1985.

Feist, C., Sotiropoulos, F., and Guala, M.: A Quasi-Coupled Wind Wave Experimental Framework for Testing Offshore Wind Turbine Floating Systems, Theoretical and Applied Mechanics Letters, 11, 100 294, https://doi.org/10.1016/j.taml.2021.100294, 2021.

https://doi.org/10.5194/wes-2026-41
Preprint. Discussion started: 17 February 2026

Fontanella, A., Bayati, I., Mikkelsen, R., Belloli, M., and Zasso, A.: UNAFLOW: A Holistic Wind Tunnel Experiment about the Aerodynamic Response of Floating Wind Turbines under Imposed Surge Motion, Wind Energy Science, 6, 1169–1190, https://doi.org/10.5194/wes-6-1169-2021, 2021.

Fu, S., Jin, Y., Zheng, Y., and Chamorro, L. P.: Wake and Power Fluctuations of a Model Wind Turbine Subjected to Pitch and Roll Oscillations, Applied Energy, 253, 113 605, https://doi.org/10.1016/j.apenergy.2019.113605, 2019.

Fu, S., Zhang, B., Zheng, Y., and Chamorro, L. P.: In-Phase and out-of-Phase Pitch and Roll Oscillations of Model Wind Turbines within Uniform Arrays, Applied Energy, 269, 114 921, https://doi.org/10.1016/j.apenergy.2020.114921, 2020.

Fu, S., Li, Z., Zhu, W., Han, X., Liang, X., Yang, H., and Shen, W.: Study on Aerodynamic Performance and Wake Characteristics of a Floating Offshore Wind Turbine under Pitch Motion, Renewable Energy, 205, 317–325, https://doi.org/10.1016/j.renene.2023.01.040, 2023.

Geibel, M. and Bangga, G.: Data Reduction and Reconstruction of Wind Turbine Wake Employing Data Driven Approaches, Energies, 15, 3773, https://doi.org/10.3390/en15103773, 2022.

Holmes, P., Lumley, J. L., and Berkooz, G.: Turbulence, Coherent Structures, Dynamical Systems and Symmetry, Cambridge University Press, ISBN 978-0-511-62270-0, 1996.

Hubert, A., Conan, B., and Aubrun, S.: Dynamic Response of a Wind Turbine Wake Subjected to Surge and Heave Step Motions under Different Inflow Conditions, Journal of Physics: Conference Series, 2767, 092 035, https://doi.org/10.1088/1742-6596/2767/9/092035, 2024a.

Hubert, A., Conan, B., and Aubrun, S.: Spatio-Temporal Behavior of the Far-Wake of a Wind Turbine Model Subjected to Harmonic Motions: Phase Averaging Applied to Stereo-PIV Measurements, https://doi.org/10.5194/wes-2024-95, 2024b.

King, L. V.: On the Convection of Heat from Small Cylinders in a Stream of Fluid: Determination of the Convection Constants of Small Platinum Wires, with Applications to Hot-Wire Anemometry, Proceedings of the Royal Society of London. Series A, Containing Papers of a Mathematical and Physical Character, 90, 563–570, https://doi.org/10.1098/rspa.1914.0089, 1914.

Kleine, V. G., Franceschini, L., Carmo, B. S., Hanifi, A., and Henningson, D. S.: The Stability of Wakes of Floating Wind Turbines, Physics of Fluids, 34, 074 106, https://doi.org/10.1063/5.0092267, 2022.

Kleusberg, E., Benard, S., and Henningson, D. S.: Tip-Vortex Breakdown of Wind Turbines Subject to Shear, Wind Energy, 22, 1789–1799, https://doi.org/10.1002/we.2403, 2019.

Kopperstad, K. M., Kumar, R., and Shoele, K.: Aerodynamic Characterization of Barge and Spar Type Floating Offshore Wind Turbines at Different Sea States, Wind Energy, 23, 2087–2112, https://doi.org/10.1002/we.2547, 2020.

Larsen, G. C., ed.: Dynamic Wake Meandering Modeling, no. 1607 in Risø R, Report, Risø National Laboratory, Roskilde, ISBN 978-87-550-3602-4, 2007.

Leimeister, M., Kolios, A., and Collu, M.: Critical Review of Floating Support Structures for Offshore Wind Farm Deployment, Journal of Physics: Conference Series, 1104, 012 007, https://doi.org/10.1088/1742-6596/1104/1/012007, 2018.

Li, Y., Yu, W., and Sarlak, H.: Wake Structures and Performance of Wind Turbine Rotor With Harmonic Surging Motions Under Laminar and Turbulent Inflows, Wind Energy, p. e2949, https://doi.org/10.1002/we.2949, 2024.

Li, Z., Dong, G., and Yang, X.: Onset of Wake Meandering for a Floating Offshore Wind Turbine under Side-to-Side Motion, Journal of Fluid Mechanics, 934, A29, https://doi.org/10.1017/jfm.2021.1147, 2022.

Lu, H. and Porté-Agel, F.: Large-Eddy Simulation of a Very Large Wind Farm in a Stable Atmospheric Boundary Layer, Physics of Fluids, 23, 065 101, https://doi.org/10.1063/1.3589857, 2011.

https://doi.org/10.5194/wes-2026-41
Preprint. Discussion started: 17 February 2026

Mendez, M. A., Balabane, M., and Buchlin, J.-M.: Multi-Scale Proper Orthogonal Decomposition of Complex Fluid Flows, Journal of Fluid Mechanics, 870, 988–1036, https://doi.org/10.1017/jfm.2019.212, 2019.

Meng, H., Su, H., Qu, T., and Lei, L.: Wind Tunnel Study on the Wake Characteristics of a Wind Turbine Model Subjected to Surge and Sway Motions, Journal of Renewable and Sustainable Energy, 14, 013 307, https://doi.org/10.1063/5.0079843, 2022.

Messmer, T., Hölling, M., and Peinke, J.: Enhanced Recovery Caused by Nonlinear Dynamics in the Wake of a Floating Offshore Wind Turbine, Journal of Fluid Mechanics, 984, A66, https://doi.org/10.1017/jfm.2024.175, 2024.

Muller, Y.-A., Aubrun, S., and Masson, C.: Determination of Real-Time Predictors of the Wind Turbine Wake Meandering, Experiments in Fluids, 56, 53, https://doi.org/10.1007/s00348-015-1923-9, 2015.

Ninni, D. and Mendez, M. A.: MODULO: A Software for Multiscale Proper Orthogonal Decomposition of Data, SoftwareX, 12, 100 622, https://doi.org/10.1016/j.softx.2020.100622, 2020.

Pedersen, J. and Meyer, K.: POD Analysis of Flow Structures in a Scale Model of a Ventilated Room, Experiments in Fluids, 33, 940–949, https://doi.org/10.1007/s00348-002-0514-8, 2002.

Porchetta, S., Temel, O., Muñoz-Esparza, D., Reuder, J., Monbaliu, J., Van Beeck, J., and Van Lipzig, N.: A New Roughness Length Parameterization Accounting for Wind–Wave (Mis)Alignment, Atmospheric Chemistry and Physics, 19, 6681–6700, https://doi.org/10.5194/acp-19-6681-2019, 2019.

Porté-Agel, F., Bastankhah, M., and Shamsoddin, S.: Wind-Turbine and Wind-Farm Flows: A Review, Boundary-Layer Meteorology, 174, 1–59, https://doi.org/10.1007/s10546-019-00473-0, 2020.

Raffel, M., Willert, C., and Kompenhans, J., eds.: Particle Image Velocimetry: A Practical Guide, Springer, Heidelberg ; New York, 1st ed edn., ISBN 3-540-63683-8, 1998.

Raibaudo, C., Gilloteaux, J.-C., and Perret, L.: Realistic Turbulent Inflow Conditions for Estimating the Performance of a Floating Wind Turbine, Wind Energy Science, 8, 1711–1725, https://doi.org/10.5194/wes-8-1711-2023, 2023.

Rockel, S., Camp, E., Schmidt, J., Peinke, J., Cal, R., and Hölling, M.: Experimental Study on Influence of Pitch Motion on the Wake of a Floating Wind Turbine Model, Energies, 7, 1954–1985, https://doi.org/10.3390/en7041954, 2014.

Schliffke, B.: Experimental Characterisation of the Far Wake of a Modelled Floating Wind Turbine as a Function of Incoming Swell, Ph.D. thesis, Centrale Nantes, Nantes, 2022.

Schliffke, B., Conan, B., and Aubrun, S.: Floating Wind Turbine Motion Signature in the Far-Wake Spectral Content – a Wind Tunnel Experiment, Wind Energy Science, 9, 519–532, https://doi.org/10.5194/wes-9-519-2024, 2024.

Sciacchitano, A.: Uncertainty Quantification in Particle Image Velocimetry, Measurement Science and Technology, 30, 092 001, https://doi.org/10.1088/1361-6501/ab1db8, 2019.

Sebastian, T. and Lackner, M.: Offshore Floating Wind Turbines - An Aerodynamic Perspective, in: 49th AIAA Aerospace Sciences Meeting Including the New Horizons Forum and Aerospace Exposition, American Institute of Aeronautics and Astronautics, Orlando, Florida, ISBN 978-1-60086-950-1, https://doi.org/10.2514/6.2011-720, 2011.

Sebastian, T. and Lackner, M.: Analysis of the Induction and Wake Evolution of an Offshore Floating Wind Turbine, Energies, 5, 968–1000, https://doi.org/10.3390/en5040968, 2012.

Sebastian, T. and Lackner, M.: Characterization of the Unsteady Aerodynamics of Offshore Floating Wind Turbines: Unsteady Aerodynamics of Offshore Floating Wind Turbines, Wind Energy, 16, 339–352, https://doi.org/10.1002/we.545, 2013.

Sirovich, L.: Turbulence and the Dynamics of Coherent Structures. II. Symmetries and Transformations, Quarterly of Applied Mathematics, 45, 573–582, https://doi.org/10.1090/qam/910463, 1987.

https://doi.org/10.5194/wes-2026-41
Preprint. Discussion started: 17 February 2026

595 VDI: Physical Modelling of Flow and Dispersion Processes in the Atmospheric Boundary Layer - Application of Wind Tunnels, Tech. Rep. 12, Engl. VDI/DIN-Kommission Reinhaltung der Luft (KRdL) - Normenausschuss, 2000.

Vermeer, L., Sørensen, J., and Crespo, A.: Wind Turbine Wake Aerodynamics, Progress in Aerospace Sciences, 39, 467–510, https://doi.org/10.1016/S0376-0421(03)00078-2, 2003.

Wieneke, B.: PIV Uncertainty Quantification and Beyond, Ph.D. thesis, Delft University of Technology,
600 https://doi.org/10.4233/UUID:4CA8C0B8-0835-47C3-8523-12FC356768F3, 2017.